

Resonant and near-resonant internal wave triads for non-uniform stratifications. Part 2. Vertically bounded domain with mild-slope bathymetry

Saranraj Gururaj^{1,†} and Anirban Guha¹

¹School of Science and Engineering, University of Dundee, Dundee DD1 4HN, UK

(Received 18 June 2021; revised 10 May 2022; accepted 10 May 2022)

Weakly nonlinear internal wave–wave interaction is a key mechanism that cascades energy from large to small scales, leading to ocean turbulence and mixing. Oceans typically have a non-uniform density stratification profile; moreover, submarine topography leads to a spatially varying bathymetry (h). Under these conditions and assuming mild-slope bathymetry, we employ multiple-scale analysis to derive the wave amplitude equations for weakly nonlinear wave–wave interactions. The waves are assumed to have a slowly (rapidly) varying amplitude (phase) in space and time. For uniform stratifications, the horizontal wavenumber (k) condition for waves (1, 2, 3), given by $k_{(1,a)} + k_{(2,b)} + k_{(3,c)} = 0$, is unaffected as h is varied, where (a, b, c) denote the mode number. Moreover, the nonlinear coupling coefficients (NLC) are proportional to $1/h^2$, implying that triadic waves grow faster while travelling up a seamount. For non-uniform stratifications, triads that do not satisfy the condition $a = b = c$ may not satisfy the horizontal wavenumber condition as h is varied, and unlike uniform stratification, the NLC may not decrease (increase) monotonically with increasing (decreasing) h . NLC, and hence wave growth rates for weakly nonlinear wave–wave interactions, can also vary rapidly with h . The most unstable daughter wave combination of a triad with a mode-1 parent wave can also change for relatively small changes in h . We also investigate higher-order self-interactions in the presence of a monochromatic, small-amplitude topography; here, the topography behaves as a zero-frequency wave. We derive the amplitude evolution equations and show that higher-order self-interactions might be a viable mechanism of energy cascade.

Key words: internal waves, stratified flows, topographic effects

† Email address for correspondence: gmsaranraj@gmail.com

1. Introduction

Low-mode long-wavelength internal gravity waves in oceans can travel thousands of kilometres from their generation site without dissipation (Zhao *et al.* 2016). The energy in these long waves can cascade to small scales through a variety of mechanisms, such as nonlinear interactions among the waves (MacKinnon & Winters 2005; MacKinnon *et al.* 2013), scattering through interaction with the seafloor topography (Legg & Adcroft 2003), and scattering through interaction with turbulent quasi-geostrophic flows (Kafiabad, Savva & Vanneste 2019). This transfer of energy to small scales will lead eventually to turbulence and mixing, which is essential for maintaining the meridional overturning circulation (Munk 1966). In weakly nonlinear wave–wave interactions, an internal gravity wave can become unstable via resonant triad interactions if it has the largest frequency in the triad (Hasselmann 1967); through this mechanism, energy is transferred irreversibly from a high-frequency and low-wavenumber primary wave to lower-frequency and higher-wavenumber secondary waves. In a resonant internal wave triad, a wave of angular frequency ω_3 and wave vector \mathbf{k}_3 can transfer its energy resonantly to two ‘daughter’ waves when both the conditions $\mathbf{k}_3 = \mathbf{k}_1 + \mathbf{k}_2$ and $\omega_3 = \omega_1 + \omega_2$ are met (Davis & Acrivos 1967; Hasselmann 1967; Phillips 1967). The former condition is a consequence of the quadratic nonlinearity of the Navier–Stokes equations.

Since ocean’s density stratification is non-uniform, recent efforts have been directed towards understanding energy transfer in non-uniformly stratified fluids. In Varma & Mathur (2017), the conditions for the existence of resonant, weakly nonlinear wave–wave interactions in a non-uniform stratification were studied. They proved that resonant triads and self-interactions can exist if (i) they satisfy the horizontal wavenumber condition, and (ii) each wave’s functional form in the z -direction is non-orthogonal to the nonlinear forcing terms. Wunsch (2017) studied self-interaction of an internal wave mode in the presence of a non-uniform stratification; the latter was simplified using a three-layer model. It was shown that the amplitude of the superharmonic wave, which is forced by the self-interaction of a parent wave, can be highly sensitive to changes in the stratification profile characteristics such as pycnocline depth and strength. Moreover, Liang, Zareei & Alam (2017) showed that self-interaction also occurs in the presence of uniform stratification, provided that the nonlinear terms in the free surface boundary condition are taken into account. Self-interaction was also studied numerically by Sutherland (2016), and it was observed that in the presence of non-uniform stratification, self-interaction of an internal wave mode was more dominant than triadic interactions for low Coriolis frequency. Furthermore, Baker & Sutherland (2020) studied self-interaction of a mode under angular frequency mismatch, and found that the daughter wave (superharmonic wave) can return its energy to the parent wave.

Apart from the weakly nonlinear wave–wave interactions, wave–topography interactions (where the topography is of small amplitude) have also been studied extensively. In Buhler & Holmes-Cerfon (2011), the decay of a mode-1 internal tide due to its interaction with a small-amplitude sea floor topography was studied using ray-tracing. It was shown that if the bottom bathymetry is ‘resonant’ (see § 6 for more detail), then the internal mode-1 wave interacts with the bathymetry and resonantly gives its energy to the higher modes. The topography in this case acts like a stationary wave with zero angular frequency. In Couston, Liang & Alam (2017), this scattering process was explored in a three-dimensional setting, where the mode-1 internal wave was incident obliquely on a small-amplitude bottom topography. Buhler & Holmes-Cerfon (2011) and Li & Mei (2014) also focused

on scattering of an internal gravity wave by a small-amplitude, stationary, zero-mean random topography. Li & Mei (2014) consider topographies that vary in zonal and meridional directions. Both studies, under realistic parameters, estimate a decay length scale of about 500–1000 km for the mode-1 wave.

In Mathur, Carter & Peacock (2014), a Green's function approach along with numerical simulations was used to study internal gravity wave scattering under the linear inviscid limit in the presence of constant and non-constant buoyancy frequency in a two-dimensional setting for large-amplitude topographies. Height of the topography and criticality (C_r) were the two main factors that influence internal gravity wave scattering. In general, subcritical ($C_r < 1$) topographies were found to scatter the incoming wave lesser than supercritical topographies ($C_r > 1$). Critical topographies ($C_r \approx 1$) were the most proficient in scattering the incoming wave. Scattering of large-amplitude waves – with breaking and the ensuing kinetic energy dissipation – is a very important quantity to study since it provides an estimate for local diffusivity. Internal wave breaking due to different types of topographies was focused on in Legg (2014). In particular, a condition for internal wave breaking was given using the incoming wave's Froude number (Fr). The Froude number for a mode-1 wave is defined as:

$$Fr = \frac{U\pi\alpha}{H\omega}, \quad (1.1)$$

where U and ω are respectively the peak horizontal velocity and frequency of the wave, H is the depth of the domain, and α is the slope of the wave. As the mode-1 wave shoals up a large-amplitude topography, its Fr increases. It is empirically determined that if a wave's Fr reaches a range 0.3–1 due to shoaling, then the wave is prone to breaking. A wave's local Froude number can also increase due to reflection from a topography. Highly nonlinear features such as bores were observed in regions of the topography where the local Froude number was greater than 1 (Legg & Adcroft 2003). Scattering and dissipation due to large-amplitude highly supercritical topographies were focused on in Klymak *et al.* (2013). Interestingly, it was observed that a mode-1 wave loses a maximum $\sim 20\%$ of its energy at an isolated tall supercritical topography.

This paper is 'Part 2' of Gururaj & Guha (2020), in which the effect of non-uniform (albeit slowly varying) stratification on internal wave triads in an unbounded domain was studied theoretically and numerically. It was shown that the variation in stratification profile may affect significantly the nonlinear coupling coefficients, (vertical wavenumber) detuning, and group speed of the wave packets constituting a triad, and hence the ensuing energy transfer. Different triads were also observed to undergo different amounts of detuning for the same change in the background stratification. The present paper extends the paradigm explored in Gururaj & Guha (2020) to a vertically bounded domain with a mild slope bathymetry, while there is no more restriction for the non-uniform stratification to be slowly varying. To the best of our knowledge, this is the first work that considers the effect of the variation of the ocean depth on internal wave triads. A simplified schematic of the set-up is given in figure 1. The motivation behind this study stems from the simple fact that ocean depth varies spatially (hence consideration of constant depth might be an over-simplification), hence waves can move from one depth to another while they are interacting in a medium of varying stratification. While the effect of change in fluid depth on resonant and near-resonant interactions between three distinct waves is the primary focus of this paper, we have also studied higher-order self-interactions among the internal waves in the presence of a small-amplitude topography. As an analogy, such higher-order interactions have been studied in Alam, Liu & Yue (2009) for surface waves. Wave-wave

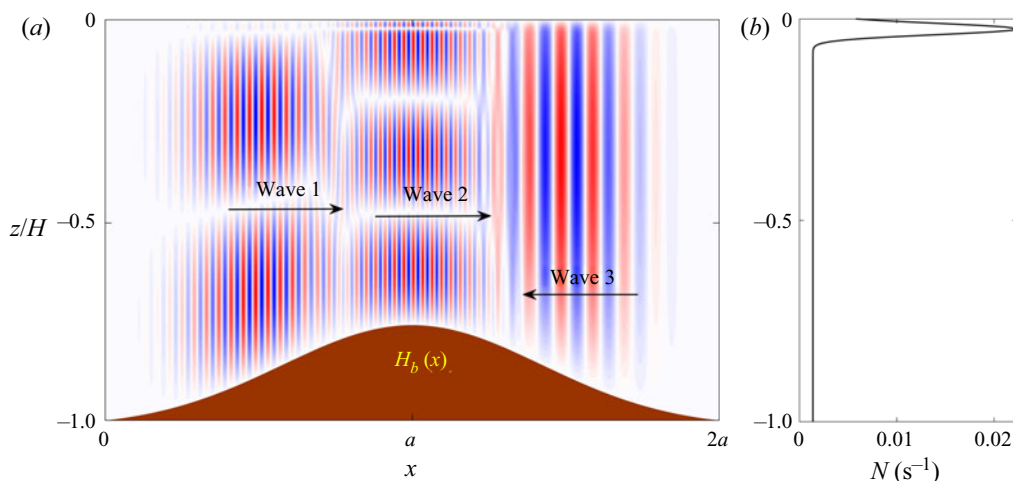


Figure 1. (a) A general schematic of the problem to be studied, showing the streamfunction field of three wave packets interacting in the presence of a varying bathymetry $h(x)$. Here, H is the mean depth (equivalent to the depth in flat bathymetry situation), while $H_b(x)$ denotes the submarine topography shape. (b) The stratification profile used in constructing the modes. The same non-uniform stratification model is used throughout the paper.

interactions in non-uniformly stratified vertically bounded domains have been considered previously in various studies (Young, Tsang & Balmforth 2008; Baker & Sutherland 2020; Varma, Chalamalla & Mathur 2020). In this paper, reduced-order models for wave–wave interactions in a region of varying h are derived, hence spatially varying nonlinear coupling coefficients, group speed and detuning are all involved. Moreover, the equations can model wave–wave interactions of wave trains or finite width wave packets in a region of varying h . In § 6, we have also derived (and validated numerically) reduced-order equations that model higher-order self-interactions in the presence of a small-amplitude topography. Equations in § 6 can also be used to model standard resonant self-interactions in the presence of slowly varying large-amplitude topographies.

The paper is organized as follows. In § 2, we derive the amplitude evolution equations of the constituent waves of a triad in the presence of a slowly varying bathymetry using the Boussinesq Navier–Stokes equations in the f -plane. To derive these equations, the streamfunction, buoyancy perturbation and meridional velocity due to each wave are assumed to be a product of a slowly varying amplitude and a rapidly varying phase that are functions of space and time. In §§ 3 and 4, the effects on the horizontal wavenumber condition when waves interact in a region of varying ocean depth in the presence of uniform and non-uniform stratification are studied, respectively. In § 5, we study the effect of ocean depth variation on the rate of energy transfer in triadic interactions and self-interactions in the presence of a non-uniform stratification. In § 6, we analyse higher-order self-interactions of a wave in the presence of small-amplitude monochromatic topography. In § 7, the reduced-order equations derived in this paper are validated by solving the full Boussinesq equations using an open source code Dedalus (Burns *et al.* 2020). The paper has been summarized in § 8.

2. Derivation of the governing equations in terrain-following coordinates

The incompressible, inviscid, two-dimensional (2-D) (in the x – z plane) Navier–Stokes equations on the f -plane under the Boussinesq approximation – hereafter referred to as

the Boussinesq equations – can be expressed in terms of the perturbation streamfunction ψ , meridional velocity v (along the y -direction), and perturbation buoyancy b as follows:

$$\frac{\partial}{\partial t}(\nabla^2\psi) + \frac{\partial b}{\partial x} - f \frac{\partial v}{\partial z} = -\{\nabla^2\psi, \psi\}, \quad (2.1a)$$

$$\frac{\partial v}{\partial t} + f \frac{\partial \psi}{\partial z} = -\{v, \psi\}, \quad (2.1b)$$

$$\frac{\partial b}{\partial t} - N^2 \frac{\partial \psi}{\partial x} = -\{b, \psi\}. \quad (2.1c)$$

Here, $N^2(z) \equiv -(g/\rho^*)(d\bar{\rho}/dz)$ is the squared buoyancy frequency, $\bar{\rho}$ is the base density profile, ρ^* is the reference density, and g is the acceleration due to gravity (directed along $-z$). The perturbation buoyancy is defined as $b \equiv -g\rho/\rho^*$, where ρ is the perturbation density.

The operator $\{G_1, G_2\} \equiv (\partial G_1/\partial x)(\partial G_2/\partial z) - (\partial G_1/\partial z)(\partial G_2/\partial x)$ denotes the Poisson bracket, and f is the Coriolis frequency. Viscous effects have been neglected owing to the fact that we consider waves with long wavelengths.

The fluid domain is bounded at the top ($z = 0$) by a rigid lid (i.e. zero vertical velocity, leading to the boundary condition $\psi(x, 0) = 0$). The bottom boundary at $z = h(x)$ satisfies the impenetrable boundary condition $\psi(x, h(x)) = 0$.

Instead of solving the fully nonlinear equations (2.1a)–(2.1c) numerically, we combine (2.1a)–(2.1c) into a single equation and employ a multiple-scale analysis. To this end, we perform $\partial(2.1a)/\partial t + f \partial(2.1b)/\partial z - \partial(2.1c)/\partial x$, which results in

$$\frac{\partial^2}{\partial t^2}(\nabla^2\psi) + N^2 \frac{\partial^2 \psi}{\partial x^2} + f^2 \frac{\partial^2 \psi}{\partial z^2} = -\frac{\partial}{\partial t}(\{\nabla^2\psi, \psi\}) + \frac{\partial}{\partial x}(\{b, \psi\}) - f \frac{\partial}{\partial z}(\{v, \psi\}). \quad (2.2)$$

Following the approach of Maugé & Gerkema (2008), we now change the governing equations to terrain-following coordinates, where a new variable (η) is defined as

$$\eta \equiv -\frac{z}{h(x)}. \quad (2.3)$$

According to the definition (2.3), the bottom boundary condition at $z = h(x)$ would now be enforced at $\eta = -1$, while the surface boundary condition at $z = 0$ remains unaltered, except that it is now at $\eta = 0$. The governing equations, which are in the x – z coordinates, need to be transformed into the x – η coordinates. The correspondences between the variables in the x – z and x – η coordinate systems are as follows:

$$\psi(x, z, t) \Rightarrow \Psi(x, \eta, t), \quad b(x, z, t) \Rightarrow B(x, \eta, t), \quad v(x, z, t) \Rightarrow \mathcal{V}(x, \eta, t). \quad (2.4a-c)$$

On transforming the differential operators from x – z coordinates to x – η coordinates and substituting the transformed variables in (2.2), we arrive at

$$\left[\frac{\partial^2}{\partial t^2} (L_{xx} + L_{\eta\eta}) + N^2(-h(x)\eta)L_{xx} + f^2 L_{\eta\eta} \right] \Psi = -\frac{\partial}{\partial t} [\mathcal{J}\{(L_{xx} + L_{\eta\eta})\Psi, \Psi\}] + L_x(\mathcal{J}\{B, \Psi\}) - f L_\eta(\mathcal{J}\{\mathcal{V}, \Psi\}), \quad (2.5)$$

where the operators $L_x, L_\eta, L_{xx}, L_{\eta\eta}$ and $\mathcal{J}\{G_1, G_2\}$ have the following definitions:

$$L_x \equiv \frac{\partial}{\partial x} + \frac{\partial \eta}{\partial x} \frac{\partial}{\partial \eta}, \quad L_\eta \equiv -\frac{1}{h} \frac{\partial}{\partial \eta}, \quad L_{\eta\eta} \equiv \frac{1}{h^2} \frac{\partial^2}{\partial \eta^2}, \quad (2.6a)$$

$$L_{xx} \equiv \frac{\partial^2}{\partial x^2} + \frac{\eta^2}{h^2} \left(\frac{\partial h}{\partial x}\right)^2 \frac{\partial^2}{\partial \eta^2} - 2 \frac{\eta}{h} \left(\frac{\partial h}{\partial x}\right) \frac{\partial^2}{\partial \eta \partial x} + \frac{\eta}{h} \left[\frac{2}{h} \left(\frac{\partial h}{\partial x}\right)^2 - \frac{\partial^2 h}{\partial x^2}\right] \frac{\partial}{\partial \eta}, \quad (2.6b)$$

$$\mathcal{J}\{G_1, G_2\} \equiv L_x(G_1) L_\eta(G_2) - L_\eta(G_1) L_x(G_2). \quad (2.6c)$$

For performing multiple-scale analysis, we assume wave-like perturbations, and the streamfunction due to the j th wave ($j = 1, 2, 3$) is given according to the following ansatz:

$$\Psi_j = a_j(\epsilon_x x, \epsilon_t t) \mathcal{E}_j(x, \eta, t) + \text{c.c.}, \quad (2.7)$$

where ‘c.c.’ denotes the complex conjugate, a_j is the slowly varying complex amplitude, and $\mathcal{E}_j(x, \eta, t)$ is the rapidly varying phase part of the j th wave. The small parameters ϵ_t and ϵ_x are respectively used to denote the weak variation of the amplitude function with time and the streamwise (x) direction. The amplitude is assumed to be an $O(\epsilon_a)$ quantity, where ϵ_a is a small parameter. The bathymetry (h), which is simply the negative of the fluid depth, is assumed to be of the form

$$h = -H + \epsilon_h H_b(k_b x), \quad (2.8)$$

where H represents the mean depth of the fluid domain, H_b denotes the submarine topography shape, ϵ_h is its amplitude, and k_b^{-1} represents the length scale of the bathymetry. We always assume the bathymetry to have a ‘mild slope’; for this we use an analogue condition of that used for surface gravity waves (Meyer 1979; Kirby 1986):

$$\frac{1}{\mathcal{K}_j} \frac{\partial h}{\partial x} = O(\epsilon_h \epsilon_k) \ll O(1), \quad (2.9)$$

where $\mathcal{K}_j \equiv k_j h$ is the non-dimensional horizontal wavenumber (k_j being the horizontal wavenumber) of the j th internal wave. Moreover, the relation $k_j^{-1} = \epsilon_k k_b^{-1}$ is used in (2.9), which implies that either of the parameters, ϵ_h or ϵ_k , could be a small quantity, while the other could potentially be an $O(1)$ quantity. We note in passing that the mild slope condition in our case can still lead to internal gravity wave scattering. Internal wave scattering is largely dependent on the slope of the wave, which is almost constant; wave slope is dependent on N , which is nearly constant away from the pycnocline – even for higher modes whose horizontal wavenumber is much larger. Scaling analysis to find the relations between these small parameters is given in [Appendix B](#).

2.1. Leading-order analysis

Next we substitute (2.7) in (2.5). At the leading order ($O(\epsilon_a)$), the governing equation (2.5) reduces to

$$\left(\frac{\partial^2}{\partial x^2} + \frac{1}{h^2} \frac{\partial^2}{\partial \eta^2}\right) \frac{\partial^2 \mathcal{E}_j}{\partial t^2} + N^2(-h(x) \eta) \frac{\partial^2 \mathcal{E}_j}{\partial x^2} + \frac{f^2}{h^2} \frac{\partial^2 \mathcal{E}_j}{\partial \eta^2} = 0. \quad (2.10)$$

Hereafter, we drop the argument of N^2 , assuming that it is implied. Furthermore, assuming $\mathcal{E}_j = \widehat{\mathcal{E}}_j(x, \eta) e^{-i\omega_j t}$, where $\omega_j \in \mathbb{R}^+$ is the angular frequency of the j th internal wave,

Effects of mild-slope bathymetry on internal wave triads

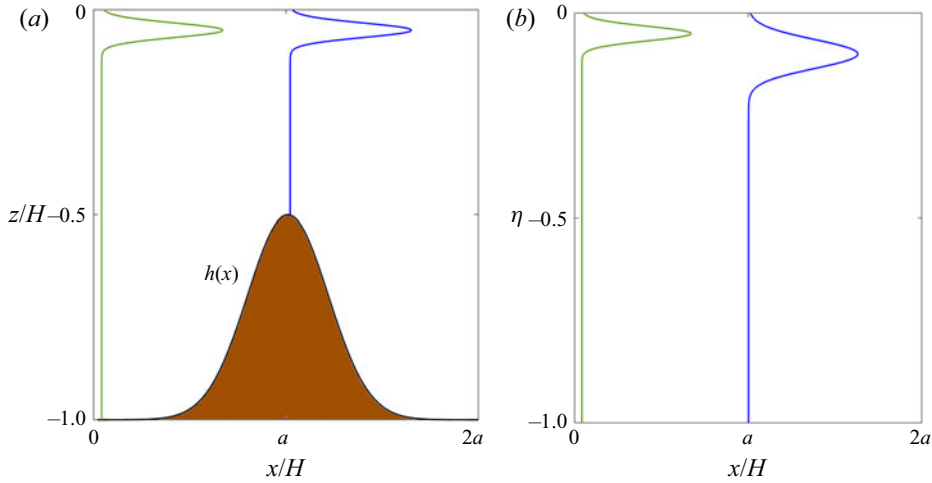


Figure 2. The effective change in the stratification profile $N(z)$ when the coordinates are changed from (a) $x-z$ to (b) $x-\eta$, in the presence of bathymetry. For the latter case, if N is a function of z in $x-z$, then it becomes a function of both η and x in $x-\eta$. The N profiles corresponding to the top of a seamount and an abyssal plain region have been denoted, respectively, by blue and green lines.

(2.10) simplifies to

$$\left[(N^2 - \omega_j^2) \frac{\partial^2}{\partial x^2} - \frac{\omega_j^2 - f^2}{h^2} \frac{\partial^2}{\partial \eta^2} \right] \widehat{\Xi}_j = 0. \tag{2.11}$$

For a mild slope bathymetry (see Appendix B for details), we can use variable separation to solve (2.11) at the leading order. To this end, we assume $\widehat{\Xi}_j = \phi_j(\eta; x) P_j(x)$, which leads to

$$\frac{h^2}{P_j} \frac{\partial^2 P_j}{\partial x^2} = \frac{\omega_j^2 - f^2}{N^2 - \omega_j^2} \frac{1}{\phi_j} \frac{\partial^2 \phi_j}{\partial \eta^2} = -\mathcal{K}_j^2, \tag{2.12}$$

where ϕ_j depends parametrically on x via h . We emphasize that in the $x-\eta$ coordinates, the presence of bathymetry makes N also a function of x ; see figure 2 for clarity.

Two separate equations, one for P_j and the other for ϕ_j , can be formed from (2.12):

$$\left[\frac{\partial^2}{\partial x^2} + \frac{\mathcal{K}_j^2}{h^2} \right] P_j = 0, \tag{2.13a}$$

$$\mathcal{L}_j \phi_j \equiv \left[\frac{\partial^2}{\partial \eta^2} + \mathcal{K}_j^2 \chi_j^2 \right] \phi_j = 0, \tag{2.13b}$$

where $\chi_j \equiv \sqrt{(N^2 - \omega_j^2)/(\omega_j^2 - f^2)}$ is defined for convenience. The boundary conditions for (2.13b) are $\phi_j = 0$ at $\eta = 0, -1$. The non-dimensional horizontal wavenumber of the j th wave, i.e. \mathcal{K}_j , is the set of eigenvalues obtained from (2.13b), which can vary in x when N is a function of x in $x-\eta$ coordinates. An important point to note is the convention used in our study. While positive (negative) k_j implies waves propagating along $+x$ ($-x$), owing to the fact that h is negative, \mathcal{K}_j follows the exact opposite convention. This means that a negative (positive) \mathcal{K}_j implies that the wave is travelling along the

+x (−x) direction. Moreover we notice that (2.13b) does not depend explicitly on h . The only way (2.13b) can be influenced by h is through N when the latter varies in the z -direction (in x - z coordinates). However, for a uniform stratification, i.e. $N = \text{constant}$, eigenvalues of (2.13b) are independent of h . In this case, the eigenvalues are given by

$$\mathcal{M}_j \equiv \mathcal{K}_j \chi_j = n\pi, \tag{2.14}$$

where $n \in \mathbb{Z}^+$. We also observe that the quantity \mathcal{M}_j behaves like the vertical wavenumber of the wave that is non-dimensionalized by the local bathymetry h .

Meanwhile, P_j at the leading order of the Wentzel–Kramers–Brillouin (WKB) approximation given by

$$P_j = \exp \left\{ i \int_0^x \frac{\mathcal{K}_j(x')}{h(x')} dx' \right\}. \tag{2.15}$$

We introduce a function $\beta_j(\epsilon_k x)$ such that P_j is corrected to P_j/β_j . This slow varying function $\beta_j(\epsilon_k x)$, which acts as a correction to the first-order WKB solution (2.15), is given in (2.22). We note in passing that P_j/β_j is still a solution of (2.13a) in the leading order even after the above-mentioned correction. To normalize the eigenfunction of the waves obtained from (2.13b), every wave’s ϕ_j is constrained to satisfy

$$\frac{1}{2} \int_{-1}^0 \frac{1}{h^2} \left[\mathcal{K}_j^2 \phi_j^2 + \left(\frac{\partial \phi_j}{\partial \eta} \right)^2 \right] \partial \eta = 1. \tag{2.16}$$

After this normalization, waves having the same amplitude (a_j) will also have the same energy density at a given h , provided that $\beta_j = 1$.

The meridional velocity and the buoyancy perturbation at the leading order can be obtained by respectively converting (2.1b) and (2.1c) into the x - η coordinates and then substituting the streamfunction ansatz (2.7):

$$\mathcal{V}_j = i \frac{f}{h\omega_j} \frac{a_j}{\beta_j} \frac{\partial \phi_j}{\partial \eta} P_j e^{-i\omega_j t} + \text{c.c.}, \tag{2.17}$$

$$B_j = i \frac{N^2}{\omega_j} \frac{a_j}{\beta_j} \frac{\partial P_j}{\partial x} \phi_j e^{-i\omega_j t} + \text{c.c.} \tag{2.18}$$

2.2. Second-order analysis

2.2.1. Amplitude evolution equations for a resonant triad in non-uniform stratification

Triad interaction between three internal waves occurs at $O(\epsilon^2)$. Below, we describe the detailed derivation that leads finally to the amplitude evolution equations (2.24a)–(2.24c) of the waves constituting a triad.

After substituting the streamfunction (2.7), meridional velocity (2.17), and buoyancy perturbation (2.18) in (2.5), the equation for the j th wave can be written as

$$a_j \frac{\mathfrak{P}_j}{\beta_j} \mathcal{L}_j \phi_j = -\mathcal{F}_j, \tag{2.19}$$

where $\mathfrak{P}_j \equiv P_j e^{-i\omega_j t}$, \mathcal{L}_j has been defined in (2.13b), and

$$\begin{aligned} \mathcal{F}_j \equiv & \underbrace{i \frac{\partial a_j}{\partial t} \left(\phi_j \mathcal{K}_j^2 - \frac{\partial^2 \phi_j}{\partial \eta^2} \right) \frac{2\omega_j}{h^2} \left(\frac{\mathfrak{P}_j}{\beta_j} \right) + 2i(N^2 - \omega_j^2) \left(\frac{\mathcal{K}_j}{h} \phi_j \frac{\partial a_j}{\partial x} \right) \left(\frac{\mathfrak{P}_j}{\beta_j} \right)}_{\text{Linear term1}} \\ & + \underbrace{i(N^2 - \omega_j^2) \frac{\mathcal{K}_j}{h} \left[2 \frac{\partial \phi_j}{\partial x} + \frac{\phi_j h}{\mathcal{K}_j} \frac{\partial}{\partial x} \left(\frac{\mathcal{K}_j}{h} \right) - \frac{2\eta}{h} \frac{\partial h}{\partial x} \frac{\partial \phi_j}{\partial \eta} - 2 \frac{\phi_j}{\beta_j} \frac{d\beta_j}{dx} \right]}_{\text{Linear term2}} \left(a_j \frac{\mathfrak{P}_j}{\beta_j} \right) - NL_j. \end{aligned} \tag{2.20}$$

Here, \mathcal{F}_j is the collection of all the linear and nonlinear (NL_j) terms at $O(\epsilon^2)$ that have the phase of the j th wave. Equation (2.19) can have a non-trivial solution when \mathcal{F}_j is orthogonal to the adjoint solutions of the linear operator \mathcal{L}_j ; this procedure is outlined in Craik (1971). The complete mathematical proof for using such a condition is given in detail in Ince (1956, §9.34). Following Craik (1971), \mathcal{F}_j is multiplied by ϕ_j (since \mathcal{L}_j is a self-adjoint operator, ϕ_j is also the solution of the adjoint of \mathcal{L}_j) and then integrated in the η direction inside the boundary limits. This results in

$$\begin{aligned} & 2 \left[i\omega_j \frac{\partial a_j}{\partial t} \left(\gamma_j^{(1)} \mathcal{K}_j^2 - \gamma_j^{(2)} \right) \frac{1}{h^2} + i\gamma_j^{(3)} \left(\frac{\mathcal{K}_j}{h} \frac{\partial a_j}{\partial x} \right) \right] \frac{\mathfrak{P}_j}{\beta_j} \\ & + i \frac{\mathcal{K}_j}{h} \left[2\gamma_j^{(4)} + \frac{h\gamma_j^{(3)}}{\mathcal{K}_j} \frac{\partial}{\partial x} \left(\frac{\mathcal{K}_j}{h} \right) - \gamma_j^{(5)} \frac{2}{h} \frac{\partial h}{\partial x} - \frac{2\gamma_j^{(3)}}{\beta_j} \frac{d\beta_j}{dx} \right] a_j \frac{\mathfrak{P}_j}{\beta_j} = \int_{-1}^0 NL_j \phi_j d\eta, \end{aligned} \tag{2.21}$$

where $\gamma_j^{(n)}$ are functions that vary in the x -direction and are obtained after integration in the η direction; $\gamma_j^{(n)}$ are provided in Appendix A. Up to this point, β_j is an arbitrary function, and for convenience, we define β_j such that the second square-bracketed term in the left-hand side of (2.21) vanishes identically. It also implies that ‘Linear term 2’ in (2.20) also vanishes identically. In mathematical terms, this means that

$$\beta_j = \exp \left\{ \int_0^x \frac{h}{2\mathcal{K}_j} \frac{1}{\gamma_j^{(3)}} \left[\left(2\gamma_j^{(4)} - \gamma_j^{(5)} \frac{2}{h} \frac{\partial h}{\partial x} \right) \left(\frac{\mathcal{K}_j}{h} \right) + \gamma_j^{(3)} \frac{\partial}{\partial x} \left(\frac{\mathcal{K}_j}{h} \right) \right] dx \right\}. \tag{2.22}$$

For constant N , β_j can be simplified analytically to $\beta_j = h(x)/h(0) = -h(x)/H$, where it is assumed that $h(0) = -H$. We note in passing that the equivalent of the β_j functions was derived in Lahaye & Llewellyn Smith (2020) using a different approach. For this particular choice of β_j , if the amplitudes a_j are x -invariant, then the energy flux will be x -invariant as well, regardless of the modal shape or depth. More importantly, a wave packet’s maximum amplitude does not change when β_j , given by (2.22), is used in (2.21). This invariance of the maximum value of the a_j with varying h is very useful in estimating wave growth rates in our study, in which a major focus is on wave interactions in a region of varying h .

Next, we outline the procedure to obtain $\int_{-1}^0 NL_j \phi_j d\eta$ in (2.21) to complete the amplitude evolution equations. The streamfunction, meridional velocity and buoyancy frequency ansatz are substituted in the nonlinear terms of (2.5). The resultant resonant

nonlinear terms, after omitting non-resonant terms, can be written in a compact form as

$$\int_{-1}^0 NL_1 \phi_1 \, d\eta = \left[\int_{-1}^0 (\widehat{NL}_{(\psi,1)} + \widehat{NL}_{(B,1)} + \widehat{NL}_{(\nu,1)}) \phi_1 \, d\eta \right] \frac{a_3 \bar{a}_2}{\beta_2 \beta_3} \mathfrak{P}_3 \bar{\mathfrak{P}}_2, \quad (2.23a)$$

$$\int_{-1}^0 NL_2 \phi_2 \, d\eta = \left[\int_{-1}^0 (\widehat{NL}_{(\psi,2)} + \widehat{NL}_{(B,2)} + \widehat{NL}_{(\nu,2)}) \phi_2 \, d\eta \right] \frac{a_3 \bar{a}_1}{\beta_1 \beta_3} \mathfrak{P}_3 \bar{\mathfrak{P}}_1, \quad (2.23b)$$

$$\int_{-1}^0 NL_3 \phi_3 \, d\eta = \left[\int_{-1}^0 (\widehat{NL}_{(\psi,3)} + \widehat{NL}_{(B,3)} + \widehat{NL}_{(\nu,3)}) \phi_3 \, d\eta \right] \frac{a_1 a_2}{\beta_1 \beta_2} \mathfrak{P}_1 \bar{\mathfrak{P}}_2. \quad (2.23c)$$

We define $NL_{(*,j)} \equiv \int_{-1}^0 \widehat{NL}_{(*,j)} \phi_j \, d\eta$ for convenience; their expressions are provided in [Appendix A](#). Note that $NL_{(*,j)}$ is used directly in the amplitude evolution equations given below in [\(2.25b\)](#).

The amplitude evolution equations for the three internal gravity waves are obtained finally after equating the left-hand side of [\(2.21\)](#) with its right-hand side, where the latter has been expressed in terms of [\(A2\)–\(A4\)](#):

$$\frac{\partial a_1}{\partial t} + c_{(x,1)}^{(g)} \frac{\partial a_1}{\partial x} = \mathfrak{N}_1 a_3 \bar{a}_2 \exp \left\{ \int_0^x i(\mathcal{K}_3 - \mathcal{K}_1 - \mathcal{K}_2)/h \, dx' + i \Delta \omega t \right\}, \quad (2.24a)$$

$$\frac{\partial a_2}{\partial t} + c_{(x,2)}^{(g)} \frac{\partial a_2}{\partial x} = \mathfrak{N}_2 a_3 \bar{a}_1 \exp \left\{ \int_0^x i(\mathcal{K}_3 - \mathcal{K}_1 - \mathcal{K}_2)/h \, dx' + i \Delta \omega t \right\}, \quad (2.24b)$$

$$\frac{\partial a_3}{\partial t} + c_{(x,3)}^{(g)} \frac{\partial a_3}{\partial x} = \mathfrak{N}_3 a_1 a_2 \exp \left\{ \int_0^x i(\mathcal{K}_1 + \mathcal{K}_2 - \mathcal{K}_3)/h \, dx' - i \Delta \omega t \right\}, \quad (2.24c)$$

where

$$c_{(x,j)}^{(g)} = \left[\frac{2i\mathcal{K}_j \mathcal{Y}_j^{(3)}}{h\mathfrak{D}_j} \right], \quad \text{in which } \mathfrak{D}_j = 2i\omega_j \left(\gamma_j^{(1)} \mathcal{K}_j^2 - \gamma_j^{(2)} \right) / h^2, \quad (2.25a)$$

$$\mathfrak{N}_j = \frac{1}{D_j} [NL_{(\nu,j)} + NL_{(B,j)} + NL_{(\psi,j)}]. \quad (2.25b)$$

In the above equation,

$$D_1 = \mathfrak{D}_1 \frac{\beta_2 \beta_3}{\beta_1}, \quad D_2 = \mathfrak{D}_2 \frac{\beta_1 \beta_3}{\beta_2}, \quad D_3 = \mathfrak{D}_3 \frac{\beta_1 \beta_2}{\beta_3}. \quad (2.26a-c)$$

The coefficient $c_{(x,j)}^{(g)}$ denotes the (weakly varying) horizontal group speed, and \mathfrak{N}_j denotes the nonlinear coupling coefficient of the j th wave; \mathfrak{N}_j determines the rate of energy transfer between the waves. Also, $\Delta\omega \equiv \omega_1 + \omega_2 - \omega_3$ denotes the detuning in the frequency. The arguments of the exponential terms in [\(2.24a\)–\(2.24c\)](#) denote both the detuning in the horizontal wavenumber condition and the frequency condition. For a pure resonant triad, $\mathcal{K}_3 - \mathcal{K}_1 - \mathcal{K}_2 = 0$ and $\Delta\omega = 0$. When $\mathcal{K}_3 - \mathcal{K}_1 - \mathcal{K}_2 \neq 0$ or $\Delta\omega \neq 0$, the triad is said to be detuned. The equations are valid only when both $\Delta\omega/\omega_j \ll 1$ and $\Delta\mathcal{K}/\mathcal{K}_j \ll 1$ are satisfied; that is, the equations are valid only in the vicinity of resonance. Analytical methods have also been developed for studying wave–wave interactions in non-resonant regimes in the presence of a slowly varying background shear flow

(e.g. Grimshaw 1988, 1994; Voelker, Akylas & Achatz 2021), where the wave train can pass through non-resonant regimes and resonant regimes. However, this is not within the scope of this paper. To summarize, amplitude (a_j) in the wave amplitude equations can vary because of the group speed term, or the nonlinear term. The group speed term is responsible for the advection of a wave packet, while the nonlinear term is responsible for energy transfer among the waves. Moreover, a wave's energy density changes because of its motion through a region of varying h . Both ϕ_j and β_j are heavily involved in the change in energy density that occurs in a wave due to its motion through a region of varying h . Note that the evolution of a_j does not provide complete information of the changes in a wave's quantities. This is because $\Psi_j = a_j\phi_j/\beta_jP_j e^{-i\omega_j t}$, where ϕ_j and β_j themselves are functions of x .

For a triad, the parent wave is always wave-3, while the daughter waves (subharmonic waves) are wave-1 and wave-2. For self-interactions, we use a different convention; see § 2.2.2. To determine how fast the daughter waves grow, a growth rate parameter σ is defined as

$$\sigma \equiv \sqrt{\mathfrak{N}_1 \mathfrak{N}_2 A_3^2}, \tag{2.27}$$

where A_3 is the parent wave's amplitude, which is held constant. To obtain this expression, the pump wave approximation of Craik, Adam & Stewartson (1978) is used. Pump wave approximation is a strong assumption that is valid only at initial times where the parent wave has much more energy than the daughter waves. Equation (2.27) reveals that the growth rate is dependent directly on the nonlinear coupling coefficients. If we ignore the nonlinear terms, then (2.24a)–(2.24c) model the movements of internal wavepackets over a mild-slope bathymetry. We emphasize here that wave scattering is not included in these equations. The amplitude variation of internal waves was analysed recently by Lahaye & Llewellyn Smith (2020) (the authors focused on internal wave scattering, which is essentially a linear mechanism). While we have restricted our study to mild-slope conditions, we have extended the previous works by including the physics of (i) finite width wave packets, (ii) nonlinearity, and (iii) detuning in the horizontal wavenumber condition, and hence investigation of both resonant (zero detuning) and near-resonant conditions. In this paper, we focus mainly on the variation of detuning, and growth rates (using pump wave approximation) with h/H for wave–wave interactions. Even though (2.24a)–(2.24c) allow finite width wave packets, we do not discuss them significantly since they have been studied in Gururaj & Guha (2020). The combined effect of nonlinear coupling coefficients, group speed and detuning has been discussed in Gururaj & Guha (2020).

The main results of scaling analysis, detailed in Appendix B, are summarized here. The relation between the small parameters is given by

$$\epsilon_t \sim \frac{\mathfrak{N}}{\omega} \epsilon_a - \widehat{c}_g \epsilon_x, \tag{2.28}$$

where \widehat{c}_g is a non-dimensional term that gives a scale of the group speed. Equation (2.28) provides the scaling for ‘Linear term 1’, and NL_j given in (2.20). These are also the final terms that are present in the wave amplitude equations (2.24a)–(2.24c). The wave amplitude (a_j) can evolve due to the group speed term or the nonlinear term. Note that if \mathfrak{N} or ϵ_a is reduced (implying that nonlinear coupling coefficients or amplitude is reduced), then we can expect nonlinear effects to decrease. However, if ϵ_x is reduced (which means that packet width is increased), then the effect of group speed, which advects the packets, is reduced.

2.2.2. Amplitude evolution equations for self-interaction in non-uniform stratification

Self-interactions can be considered as a special case of triad interactions. During resonant self-interactions, an internal wave gives its energy spontaneously to another internal wave that has twice its frequency and horizontal wavenumber (Wunsch 2017). In non-uniform stratification, a resonant self-interaction occurs when both (ω, k) and $(2\omega, 2k)$ satisfy the dispersion relation. The evolution equations for the self-interaction of a mode can be obtained from (2.24a)–(2.24c) after some straightforward modifications. The complete set of governing equations for the self-interaction of a mode in the presence of a mild-slope bathymetry h is

$$\frac{\partial a_{(3,s)}}{\partial t} + c_{(x,3)}^{(g)} \frac{\partial a_{(3,s)}}{\partial x} = \mathcal{N}_3 a_{(1,s)}^2 \exp \left\{ \int_0^x i(2\mathcal{K}_1 - \mathcal{K}_3)/h dx' - i \Delta\omega_s t \right\}, \quad (2.29a)$$

$$\frac{\partial a_{(1,s)}}{\partial t} + c_{(x,1)}^{(g)} \frac{\partial a_{(1,s)}}{\partial x} = \mathcal{N}_1 a_{(3,s)} \bar{a}_{(1,s)} \exp \left\{ \int_0^x i(\mathcal{K}_3 - 2\mathcal{K}_1)/h dx' + i \Delta\omega_s t \right\}, \quad (2.29b)$$

where the subscript ‘s’ denotes self-interaction. Moreover, $\Delta\omega_s = 2\omega_1 - \omega_3$. Unlike the triad case, the parent wave for self-interaction is wave-1, while the daughter (superharmonic) wave is wave-3. The notation throughout this paper follows the convention that wave-3 always has the highest frequency (hence for triads, wave-3 becomes the parent wave). The functions $c_{(x,j)}^{(g)}$ are the same as the expressions given in (2.25a). The functions \mathcal{N}_j , which are the nonlinear coupling coefficients for the self-interaction process, are given by

$$\mathcal{N}_1 = \mathfrak{N}_2, \quad (2.30a)$$

$$\mathcal{N}_3 = \frac{2\mathcal{K}_1^3}{h^4 \mathcal{D}_3} \left(\frac{\Gamma^{(4)}}{\omega_1} \right) - \frac{2f^2}{h^4 \mathcal{D}_3} \left(\frac{\Gamma_1^{(3)} \mathcal{K}_1}{\omega_1} \right) + \frac{\mathcal{K}_1 \omega_3}{h^4 \mathcal{D}_3} \left(\zeta_1 \omega_1^2 \Gamma_1^{(1)} - \zeta_1 \Gamma_1^{(2)} - \Gamma_1^{(3)} \right), \quad (2.30b)$$

where $\zeta_j \equiv \mathcal{K}_j^2 / (\omega_j^2 - f^2)$ is defined for convenience. Here, all Γ, \mathcal{D}_j terms in (2.30a) and (2.30b) are evaluated using (A5) and (2.26a–c) by simply considering all ‘2’ subscripts as ‘1’ – for example, substituting β_1 for β_2 in \mathcal{D}_j , and similarly substituting ϕ_1 for ϕ_2 in Γ expressions. This is because in self-interaction, wave-2 is the same as wave-1.

Equations (2.29a)–(2.29b) can predict the growth of the daughter wave and the consequent decay of the parent wave. For obtaining the growth rate of the daughter waves, we use the pump wave approximation and hence treat the parent wave’s amplitude $a_{(1,s)}$ as constant. This yields (assuming plane waves in the x -direction)

$$a_{(3,s)} = \left[\mathcal{N}_3 a_{(1,s)}^2 \right] t, \quad (2.31)$$

where the term in square brackets denotes the growth rate. From this equation it is evident that \mathcal{N}_3 acts as a proxy to the growth rate.

2.3. Energy evaluation

The time-averaged energy density for an internal gravity wave over its time period is given by

$$\langle TE_j \rangle = \frac{\omega_j}{2\pi} \int_0^{2\pi/\omega_j} \frac{\rho_0}{2} \left[\left(\frac{\partial \psi_j}{\partial z} \right)^2 + \left(\frac{\partial \psi_j}{\partial x} \right)^2 + v_j^2 + \frac{b_j^2}{N^2} \right] dt. \quad (2.32)$$

The domain-integrated total energy is given by

$$\widehat{TE}_j = \int_0^D \int_h^0 \langle TE_j \rangle dz dx = \int_0^D \int_{-1}^0 \langle TE_j \rangle (-h(x)) d\eta dx. \quad (2.33)$$

After some simplification, we arrive at

$$\widehat{TE}_j = \int_0^D \int_{-1}^0 -\frac{2}{h} \left[\mathcal{K}_j^2 \phi_j^2 + \left(\frac{\partial \phi_j}{\partial \eta} \right)^2 \right] |a_j|^2 \frac{\rho_0}{\beta_j^2} d\eta dx, \quad (2.34)$$

where D is the length of the domain in the x -direction. We non-dimensionalize \widehat{TE}_j with the initial energy of the parent wave (abbreviated as ‘ Pw ’): $E_j = \widehat{TE}_j / \widehat{TE}_{Pw}|_{t=0}$. Note that $Pw = 3$ (i.e. wave-3) for triads, and $Pw = 1$ (i.e. wave-1) for self-interactions.

3. Triad interactions in a uniform stratification in the presence of a mild-slope bathymetry

In this section, we consider resonant and near-resonant triads in a uniform background stratification in the presence of a mild-slope bathymetry. Here, we will consider briefly the horizontal wavenumber triad condition in uniform stratification as h is varied. Without any loss of generality, the triad condition for the horizontal wavenumber is

$$\mathcal{K}_3 = \mathcal{K}_1 + \mathcal{K}_2. \quad (3.1)$$

However, using (2.13b), it can be seen that the \mathcal{K}_j are constants for uniform stratification. As a result, triad conditions are satisfied everywhere in the domain, provided that the conditions are satisfied perfectly for any given domain height.

3.1. Effect of bathymetry on the nonlinear coupling coefficients of resonant triads

Here, we focus on the nonlinear coupling coefficients in resonant triad interactions (i.e. no detuning) in the presence of a uniform stratification and a weakly varying bathymetry. Equation (2.27) revealed that the growth rate of the daughter waves is dependent on the nonlinear coupling coefficients. For constant N , the nonlinear coupling coefficients (\mathfrak{N}_j) in (2.25b) can be further simplified as

$$\begin{aligned} \mathfrak{N}_1 = & \frac{iH}{2h^2 \omega_1 \kappa_1 \kappa_2 \kappa_3} \left[N^2 (\mathcal{K}_3 - \mathcal{K}_2) \left\{ \left(\frac{\mathcal{K}_3}{\omega_3} - \frac{\mathcal{K}_2}{\omega_2} \right) (\mathcal{K}_2 \mathcal{M}_3 - \mathcal{K}_3 \mathcal{M}_2) \right\} \right. \\ & + \omega_1 \left\{ (\mathcal{K}_2 \mathcal{M}_3 - \mathcal{K}_3 \mathcal{M}_2) \left(\mathcal{M}_2^2 + \mathcal{K}_2^2 - \mathcal{K}_3^2 - \mathcal{M}_3^2 \right) \right\}, \\ & \left. + f^2 (\mathcal{M}_3 - \mathcal{M}_2) \left\{ \left(\frac{\mathcal{K}_3}{\omega_3} + \frac{\mathcal{K}_2}{\omega_2} \right) (\mathcal{M}_3 \mathcal{M}_2) - \left(\frac{\mathcal{K}_2}{\omega_3} + \frac{\mathcal{K}_3}{\omega_2} \right) (\mathcal{M}_2^2 + \mathcal{M}_3^2) \right\} \right], \end{aligned} \quad (3.2a)$$

$$\begin{aligned} \mathfrak{N}_2 = & \frac{iH}{2h^2\omega_2\kappa_1\kappa_2\kappa_3} \left[N^2(\mathcal{K}_3 - \mathcal{K}_1) \left\{ \left(\frac{\mathcal{K}_3}{\omega_3} - \frac{\mathcal{K}_1}{\omega_1} \right) (\mathcal{K}_1\mathcal{M}_3 - \mathcal{K}_3\mathcal{M}_1) \right\} \right. \\ & + \omega_2 \left\{ (\mathcal{K}_1\mathcal{M}_3 - \mathcal{K}_3\mathcal{M}_1) (\mathcal{M}_1^2 + \mathcal{K}_1^2 - \mathcal{K}_3^2 - \mathcal{M}_3^2) \right\}, \\ & \left. + f^2 (\mathcal{M}_3 - \mathcal{M}_1) \left\{ \left(\frac{\mathcal{K}_1}{\omega_1} + \frac{\mathcal{K}_3}{\omega_3} \right) (\mathcal{M}_1\mathcal{M}_3) - \left(\frac{\mathcal{K}_1}{\omega_3} + \frac{\mathcal{K}_3}{\omega_1} \right) (\mathcal{M}_1^2 + \mathcal{M}_3^2) \right\} \right], \end{aligned} \tag{3.2b}$$

$$\begin{aligned} \mathfrak{N}_3 = & \frac{iH}{2h^2\omega_3\kappa_1\kappa_2\kappa_3} \left[N^2(\mathcal{K}_1 + \mathcal{K}_2) \left\{ \left(\frac{\mathcal{K}_1}{\omega_1} - \frac{\mathcal{K}_2}{\omega_2} \right) (\mathcal{K}_2\mathcal{M}_1 - \mathcal{K}_1\mathcal{M}_2) \right\} \right. \\ & + \omega_3 \left\{ (\mathcal{K}_2\mathcal{M}_1 - \mathcal{K}_1\mathcal{M}_2) (\mathcal{M}_1^2 + \mathcal{K}_1^2 - \mathcal{K}_2^2 - \mathcal{M}_2^2) \right\} \\ & \left. + f^2 (\mathcal{M}_1 + \mathcal{M}_2) \left\{ \left(\frac{\mathcal{K}_1}{\omega_2} + \frac{\mathcal{K}_2}{\omega_1} \right) (\mathcal{M}_1^2 + \mathcal{M}_2^2) - \left(\frac{\mathcal{K}_1}{\omega_1} + \frac{\mathcal{K}_2}{\omega_2} \right) (\mathcal{M}_1\mathcal{M}_2) \right\} \right], \end{aligned} \tag{3.2c}$$

where $\kappa_j = \sqrt{\mathcal{M}_j^2 + \mathcal{K}_j^2}$. Note that the above expressions are obtained only when the vertical wavenumber condition is satisfied. The terms inside the square brackets are constant and hence do not vary with the bathymetry h . The fact that \mathcal{K}_j and \mathcal{M}_j are constants for a constant N is given in (2.14). For constant N , $\beta_j = -h(x)/H$, which has been used in (3.2a)–(3.2c), and this results finally in $\mathfrak{N}_j \propto 1/h^2$. Hence for waves travelling from a given fluid depth to a lesser depth (i.e. as the waves climb up a seamount), the nonlinear coupling coefficients, and hence the growth rates, increase following the inverse square rule.

In summary, for a uniform stratification, if three modes satisfy the resonant triad condition at a particular domain height, then they would satisfy the resonant triad condition for any domain height. Moreover, we also showed that the nonlinear coupling coefficients increase (decrease) as the fluid depth decreases (increases) following an inverse square law.

4. Triad interactions and self-interactions in a non-uniform stratification in the presence of a mild-slope bathymetry: detuning effects

In § 3, it was shown that in the presence of a uniform stratification, if the triad condition is satisfied between three modes at a particular h , then it is satisfied for all h . However, in non-uniform stratification, such a simple outcome is not possible. In certain types of triads, there can be a heavy mismatch in the horizontal wavenumber condition as the waves involved in the triad interact in a region of varying domain height. This may affect the energy transfer between the waves.

In this section, we study the factors that decide the detuning (or mismatch) between the horizontal wavenumber of the waves as h is varied in the presence of non-uniform stratification. Here, as well as in the rest of this paper, we will consider a Gaussian function to represent the buoyancy frequency

$$N(z) = N_b + N_{max} \exp \left[- \left\{ (z - z_c) / W_p \right\}^2 \right], \tag{4.1}$$

where the parameters N_b , N_{max} , W_p and z_c are varied. This kind of profile (see figure 1b) is a simplified representation of oceanic stratification and is used widely in the literature; see

Grisouard, Staquet & Gerkema (2011), Mathur *et al.* (2014) and Varma & Mathur (2017). We choose stratification profiles such that the pycnocline is above the topography. If the topography cuts the pycnocline, then internal wave scattering may be significant, as shown in Hall, Huthnance & Williams (2013).

4.1. *Effect of varying h on the horizontal wavenumber condition for waves satisfying $f \ll \omega_j \ll N_b$*

First, we study the class of triads for which the angular frequencies of the constituent waves obey the condition $f \ll \omega_j \ll N_b$. It is assumed that the parent wave (angular frequency ω_3) gives its energy to two subharmonic daughter waves of angular frequencies ω_1 and ω_2 , respectively; that is, the conditions $\omega_1 < \omega_3$ and $\omega_2 < \omega_3$ are always assumed. A parameter $\alpha \in (0, 1)$ is defined such that $\omega_1 = \alpha\omega_3$ and $\omega_2 = (1 - \alpha)\omega_3$. Two different types of interactions, Class-1 and Class-2, are defined for which a parent wave can form a triad with the subharmonic daughter waves.

4.1.1. *Class-1 interactions*

We consider three waves with angular frequencies $\omega_3, \omega_1, \omega_2$ such that $\omega_3 = \omega_1 + \omega_2$. Furthermore, we assume that at a particular h , the horizontal wavenumber condition is satisfied between mode i of wave-1, mode j of wave-2, mode k of wave-3, i.e.

$$\mathcal{K}_{3(k)} = \mathcal{K}_{1(i)} + \mathcal{K}_{2(j)}, \tag{4.2}$$

where i, j and k are not all equal. This constitutes a Class-1 interaction. Now, if the stratification profile changes (the stratification profile will change in $x-\eta$ coordinates provided that h is varying), then the wavenumbers $\mathcal{K}_{1(i)}, \mathcal{K}_{2(j)}, \mathcal{K}_{3(k)}$ will also change. However, for a given change in h , all the wavenumbers may not change in a way such that condition (4.2) is satisfied. For example, if $\mathcal{K}_{1(i)} = \text{func}(h)$, then it is possible that $\mathcal{K}_{2(j)} \neq c \text{func}(h)$, where c and $\text{func}()$ denote an arbitrary constant and function, respectively. Therefore, even though the triad condition may be satisfied at a particular h , it may not be satisfied for all h . Hence Class-1 triads might get detuned as they interact in a region of varying h .

To measure the detuning (or mismatch) in the horizontal wavenumber, we define a new variable $\Delta\mathcal{K}$:

$$\Delta\mathcal{K} \equiv \frac{\mathcal{K}_{3(k)} - \mathcal{K}_{1(i)} - \mathcal{K}_{2(j)}}{\mathcal{K}_{min}}, \tag{4.3}$$

where \mathcal{K}_{min} is the minimum wavenumber of the three wavenumbers at a particular x -coordinate. This $\Delta\mathcal{K}$ acts basically as a non-dimensional measure of the detuning between the waves, and for a resonant triad, $\Delta\mathcal{K} = 0$.

We now study how different (non-dimensional) wavenumbers $\mathcal{K}_{3(n)}$ of frequency ω_3 change as h is varied in the presence of a non-uniform stratification. To obtain $\mathcal{K}_{3(n)}$ for a given stratification profile, we solve (2.13b) for $h/H \in [-1, -0.2]$. The functional form of h , as long as it is mildly varying, does not influence the wavenumbers or detuning at a particular h . The non-uniform stratification profile given by (4.1) is used throughout this paper. The stratification profiles are chosen such that $N_{max} = (2N_b, 4N_b, \dots, 12N_b)$, $W_p = (H/200, 2H/200, \dots, 5H/200)$ and $z_c = (H/80, H/40, H/20, H/10)$; and we consider all possible (120) combinations. Moreover, $\omega_3 = 0.1N_b$ and $f = 0$ are used consistently for all combinations. Figure 3 shows the variation of $\widehat{\mathcal{K}}_{3(n)} \equiv \mathcal{K}_{3(n)}(h)/\mathcal{K}_{3(n)}(H)$ with h/H for different modes n . Figures 3(a-c)

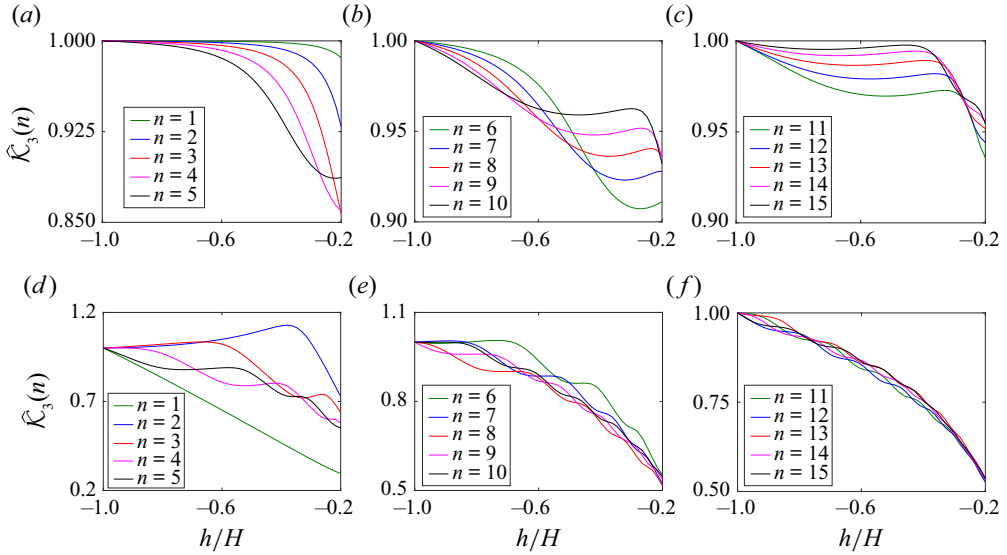


Figure 3. Variation of $\widehat{\mathcal{K}}_{3(n)}$ with h/H for two different stratification profiles. For stratification profile $N^{(1)}$: (a) modes 1–5, (b) modes 6–10, and (c) modes 11–15. For stratification profile $N^{(2)}$: (d) modes 1–5, (e) modes 6–10, and (f) modes 11–15.

uses the stratification profile $N^{(1)}$ with the parameters $N_{max} = 2N_b$, $W_p = H/200$ and $z_c = H/80$; figures 3(d–f) use the profile $N^{(2)}$ given by $N_{max} = 10N_b$, $W_p = H/50$ and $z_c = H/10$. Note that $N^{(1)}$ has a sharp pycnocline, while $N^{(2)}$ has a larger W_p resulting in a wider pycnocline. For profiles where all three parameters are low (e.g. $N^{(1)}$), $\widehat{\mathcal{K}}_{3(1)}$ is nearly constant for some range of h/H and then starts decreasing. This can be seen in figure 3(a), where the first five modes exhibit this behaviour. Moreover, for profiles where all z_c , W_p , N_{max} are high (e.g. $N^{(2)}$), $\widehat{\mathcal{K}}_{3(1)}$ decreases almost linearly with h/H , as can be seen clearly in figure 3(d). For any profile, $\widehat{\mathcal{K}}_{3(1)}$ always monotonically decreases as the fluid depth is reduced for $h/H \in [-1, -0.2]$. However, this behaviour does not hold for any mode other than mode-1. For example, for $z_c = H/10$ (regardless of W_p , N_{max}), $\widehat{\mathcal{K}}_{3(2)}$ increases for some h/H as fluid depth is reduced; see figure 3(d) (blue curve). Similar behaviour is observed for modes 3, 4 and 5 when W_p is low. In summary, the variation of $\widehat{\mathcal{K}}_{3(1)}$ with h/H can be different from that of the higher mode’s wavenumber, which can result in detuning.

For profiles with high W_p , the $\widehat{\mathcal{K}}_{3(n)}$ for $n > 10$ start to collapse on each other; see figure 3(f). In such scenarios, since $\widehat{\mathcal{K}}_{3(n)}$ remains nearly the same, $\Delta\mathcal{K}$ will not be induced by the difference in higher modes’ $\widehat{\mathcal{K}}_{3(n)}$. In general, it was observed that as W_p is reduced, n has to be higher for the modes to collapse on each other.

The interaction of a mode-1 internal wave (wave-3) with different modes in the presence of two different non-uniform stratification profiles is considered next. These profiles are a part of the 120 profiles that we mentioned already. Sample results are shown in figure 4 in which the frequencies and stratification profile parameters are as follows:

- (i) $N^{(3)}$: $\omega_3 = 0.1N_b$, $f = 0$, $N_{max} = 10N_b$, $W_p = H/100$ and $z_c = H/10$;
- (ii) $N^{(4)}$: $\omega_3 = 0.1N_b$, $f = 0$, $N_{max} = 10N_b$, $W_p = H/50$ and $z_c = H/20$.

Effects of mild-slope bathymetry on internal wave triads

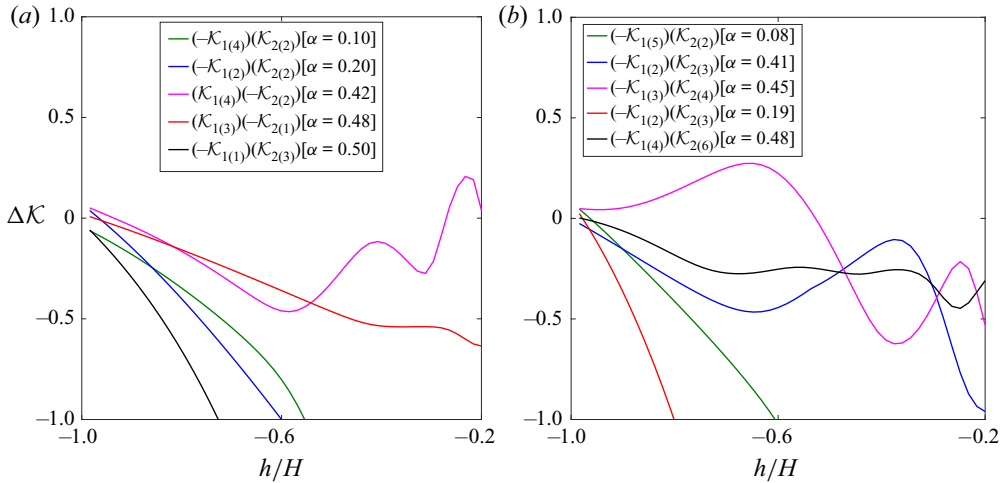


Figure 4. Variation of detuning ($\Delta\mathcal{K}$) with h/H for various modal interactions pertaining to the stratification profiles (a) $N^{(3)}$, and (b) $N^{(4)}$. The legends indicate what daughter waves were involved in the triad interactions, where $\alpha \equiv \omega_1/\omega_3$.

For each profile, we have shown five different modal interactions. Figure 4 reveals clearly that the detuning can be quite sensitive to the changes in the domain height.

4.1.2. Class-2 interactions: a special case of triad interactions

The interaction in Class-2 is between the n th modes (where $n \in \mathbb{Z}^+$) of different waves constituting a triad. For example, if mode-1 with frequency ω_1 , mode-1 with frequency ω_2 , and mode-1 with frequency ω_3 form a triad, then it is classified as a Class-2 interaction. This kind of triad is possible when $f \ll \omega_j \ll N_b$. To show how this interaction is possible, we consider the eigenproblem concerning the n th mode of the j th wave:

$$\frac{\partial^2 \phi_{j(n)}}{\partial \eta^2} + \mathcal{K}_{j(n)}^2 \chi_j^2 \phi_{j(n)} \approx \frac{\partial^2 \phi_{j(n)}}{\partial \eta^2} + \left(\frac{\mathcal{K}_{j(n)}}{\omega_j}\right)^2 N^2 \phi_{j(n)} = 0, \tag{4.4}$$

where we used $\chi_j \approx N/\omega_j$ (under the approximation $f \ll \omega_j \ll N_b$), and the system is solved using the boundary conditions $\phi_{j(n)} = 0$ at $\eta = 0$ and $\eta = -1$. However, by Sturm–Liouville theory, for a given operator (here $\partial^2/\partial \eta^2$) and weight function (here $N(z)^2$), the n th eigenvalue (here $\mathcal{K}_{j(n)}/\omega_j$) is unique, i.e. $\mathcal{K}_{j(n)}/\omega_j = \text{constant}$ for all j . Therefore, if the triad condition for frequency $\omega_3 = \omega_2 + \omega_1$ is valid, then this implies automatically the validity of the wavenumber condition $\mathcal{K}_{3(n)} = \mathcal{K}_{1(n)} + \mathcal{K}_{2(n)}$.

The situation mentioned above is true for all stratification profiles satisfying $f \ll \omega_j \ll N(z)$ (at all z -locations). This is especially important because in the presence of a bathymetry, the stratification profile changes in the x -direction in x - η coordinates. However, for Class-2 interaction, all three non-dimensional wavenumbers (eigenvalues) are the same functions of h since they are the same eigenvalues divided by their frequency. Thus the resonant triad condition will be still be satisfied even if h is varied significantly (i.e. variation of h will not cause detuning). Note that in the parameter regime $f \ll \omega_j \ll N(z)$, only Class-2 self-interactions were observed in numerical experiments of Sutherland (2016), hence Class-2 triads may always be dominated by self-interactions, resulting in the

parent wave's energy transfer to the superharmonics instead of subharmonics. As a result, Class-2 triads may not be as relevant practically as Class-2 self-interactions.

4.2. *Effect of bathymetry on horizontal wavenumber condition for Class-1 self-interaction*

Detuning can also be introduced during a self-interaction process as h is varied. Following the same terminology as before, we classify self-interactions as Class-1 and Class-2. As shown by Wunsch (2017), Class-2 self-interactions will always be slightly detuned, where the detuning increases as f increases. This is due to the fact that in a non-uniform stratification, if the n th mode of ω satisfies the dispersion relation, then the n th mode of 2ω will be able to satisfy it only approximately.

Following (4.3), the detuning for a self-interaction process is defined as

$$\Delta\mathcal{K}_s = \frac{\mathcal{K}_{3(k)} - 2\mathcal{K}_{1(i)}}{\mathcal{K}_{1(i)}}, \tag{4.5}$$

where wave-3 is the superharmonic (daughter) wave, while wave-1 is the parent wave, i.e. $\omega_1 = \omega_3/2$ (following the convention used throughout this paper that wave-3 has the highest frequency). The amplitude evolution equations for a self-interaction process are discussed in § 2.2.2.

For the range $f \ll \omega_j \ll N(z)$, the Class-2 self-interaction process will follow principles similar to those outlined in § 4.1.2. As mentioned in § 4.1.2, significant variations in h for this frequency range will not introduce detuning in Class-2 self-interactions. We now study the other end of the parameter space, where $(N^2 - \omega_j^2) \approx N^2$, which was the basic approximation used in much of our analysis in § 4.1, is no longer valid. Hence out of Class-1 and Class-2 self-interactions, only the latter are possible. This would mean that as the domain height changes, the detuning introduced could be significant. Interestingly, though, if the wavenumbers involved in the self-interaction change with h/H in a similar way, then the detuning is insignificant; see figure 5. The frequencies and the stratification profile parameters used here are:

- (i) $N^{(6)}$: $N_{max} = 10N_b$, $W_p = H/100$ and $z_c = H/10$;
- (ii) $N^{(7)}$: $N_{max} = 10N_b$, $W_p = H/100$ and $z_c = H/20$;

and $f = 0$ always. Figure 5(a) uses the set $N^{(6)}$, and shows the variation of the horizontal wavenumber of mode-2 ($\omega_3 = 0.89N_b$) and mode-3 ($\omega_1 = \omega_3/2$). These modes satisfy the condition for resonant self-interaction. We observe that these two wavenumbers behave quite similarly for a wide range of h/H , hence the detuning, shown in figure 5(b), is small (and constant for an appreciable range), in spite of the fact that it is a Class-1 interaction. The same phenomenon is also shown for several other self-interaction combinations in figure 5(c), where the parameter set $N^{(7)}$ is used.

The detuning for all the combinations shown stays constant for a certain range of h/H . We note in passing that Class-1 triad interactions may also give rise to a small detuning for a range of h/H , provided that all the modes involved behave in a similar way. However, this is a more stringent condition than a self-interaction process, where only two waves are involved. Even though equations derived in § 2 are valid only when $\Delta\mathcal{K} \ll 1$ (or $\Delta\mathcal{K}_s \ll 1$), there are a significant number of interactions where $\Delta\mathcal{K}$, or $\Delta\mathcal{K}_s$, is a small quantity even for $O(1)$ changes in depth and the wavenumber. For example, for interactions shown in this section, and for Class-2 interactions, detuning can stay as a small quantity even for

Effects of mild-slope bathymetry on internal wave triads

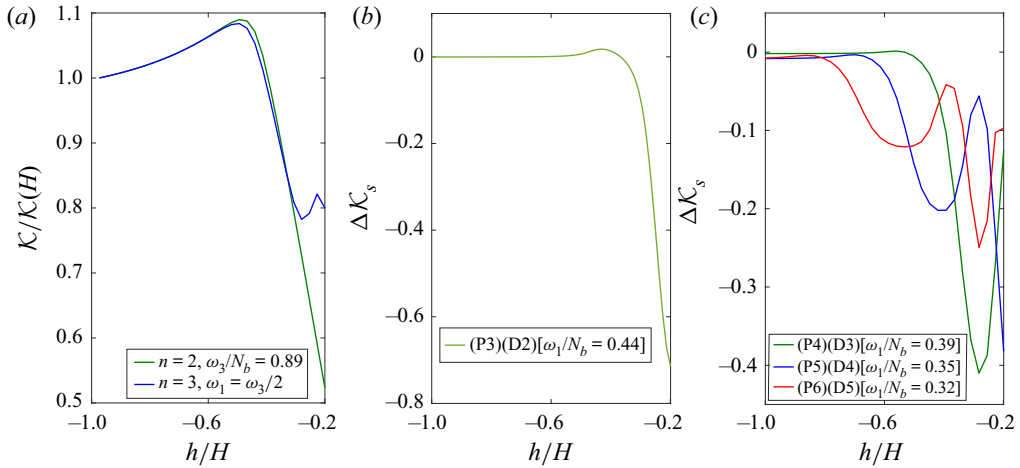


Figure 5. (a) Variations of $\mathcal{K}_{3(2)}$ and $\mathcal{K}_{1(3)}$ with h/H for the parameter set $N^{(6)}$. (b) Variation of detuning with h/H for the same case. (c) The detuning for three different self-interaction combinations for the parameter set $N^{(7)}$. Here, the notation (Pa)(Db) implies ‘Parent wave’ with mode-a, and ‘Daughter wave’ with mode-b.

$O(1)$ changes in depth. However, we do note that in several triad interactions, detuning can be sensitive to h , and in those cases, $O(1)$ changes in depth cannot be modelled accurately by the wave amplitude equations.

To summarize, in the presence of a non-uniform stratification, we divide triad and self-interactions into two classes: Class-1 and Class-2. Class-1 interactions contain waves whose mode numbers are not all the same, while Class-2 interactions contain waves that are the n th modes of their respective frequencies. Class-1 interactions may undergo detuning with the variation in h , irrespective of the frequency. However, interestingly, certain Class-1 self-interactions do not undergo detuning as h is varied inside a certain range. For both triads and self-interactions, Class-2 interactions can exist only for $f \ll \omega_j \ll N(z)$, and do not get detuned as h is varied.

5. Variation of growth rates and nonlinear coupling coefficients with depth for non-uniform stratification

In this section, we focus on the effects of domain height variation on the growth rate (σ) of triads, and the nonlinear coupling coefficient \mathcal{N}_3 , which provides a measure of the growth of the daughter wave in a self-interaction. The non-uniform stratification profile (4.1) will be used in this section.

5.1. Variation of growth rates with domain height for triads

Triad interactions are important for the decay of internal waves near the 28.9° latitude (MacKinnon & Winters 2005; MacKinnon *et al.* 2013), specifically the mode-1 wave, which is the most energy containing mode (Vic *et al.* 2019). Here, we study this phenomenon in the high-latitude region ($f/\omega_3 \geq 0.3$) for varying $N(z)$ and h . The mode-1 wave (which, being the parent wave, is wave-3) can decay forming various triad combinations; we restrict the subharmonic daughter waves (wave-1 and wave-2) up to mode-50. Moreover, for studying growth rates in the presence of varying h , the triads are identified separately at different h/H . This is because a triad combination at a particular

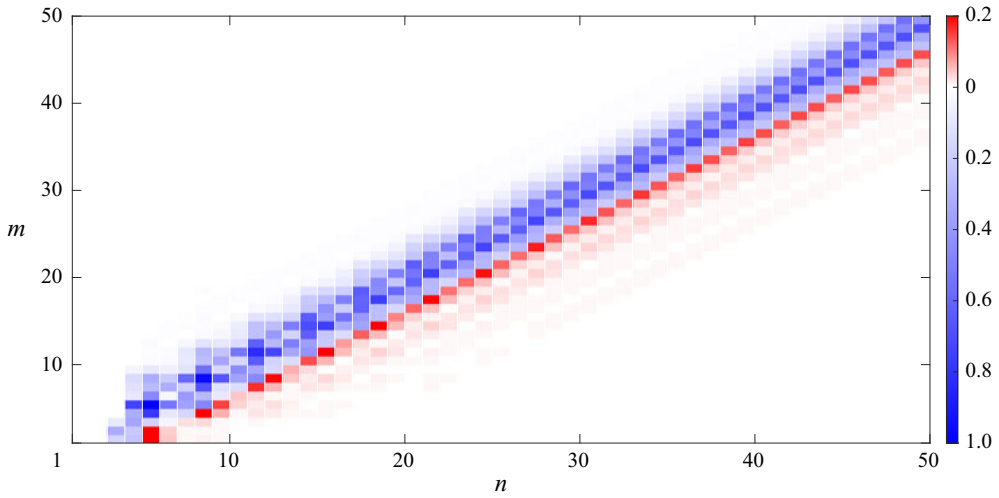


Figure 6. Contours of non-dimensional growth rate (σ/σ_{ref}) of triads formed between mode- n , mode- m and mode-1 (i.e. wave-3). Blue and red, respectively, represent Branch-1 and Branch-2 triads, and both colours represent positive values. For Branch-1 triads, mode- $m(n)$ is wave-1(2), while for Branch-2 triads, mode- $n(m)$ is wave-1(2).

h/H value may not satisfy the horizontal wavenumber condition at a different h/H (as explained in § 4). Three main branches of triads are considered here for the mode-1 internal wave:

$$\underbrace{|\mathcal{K}_3| = |\mathcal{K}_2| - |\mathcal{K}_1|}_{\text{Branch-1}} \quad \text{or} \quad \underbrace{|\mathcal{K}_3| = |\mathcal{K}_1| - |\mathcal{K}_2|}_{\text{Branch-2}} \quad \text{or} \quad \underbrace{|\mathcal{K}_3| \approx |\mathcal{K}_1| + |\mathcal{K}_2|}_{\text{Branch-3}}. \quad (5.1)$$

For Branch-1(2) triads, the wavenumber of wave-2(1) is larger in magnitude than that of wave-1(2). The only possible Branch-3 interaction is a Class-2 interaction, where both the daughter waves are also mode-1 of their respective frequencies. However, this interaction, like the Class-2 self-interaction, also undergoes heavy detuning for high f values. Therefore, Branch-3 being an inefficient energy transfer pathway, we restrict our focus to Branch-1 and Branch-2. Triads are studied for $f/\omega_3 = (0.3, 0.4, 0.45)$ in the presence of various stratification profiles. The triads are computed for $\alpha \in [0.31, 0.5]$, $\alpha \in [0.41, 0.5]$ and $\alpha \in [0.455, 0.5]$ for $f/\omega_3 = 0.3, 0.4$ and 0.45 , respectively (see § 4.1 for the definition of α).

Figure 6 shows the non-dimensionalized growth rate contour for a mode-1 wave. All growth rates σ are non-dimensionalized with a reference growth rate value σ_{ref} , where the latter denotes the maximum growth rate for all Branch-1 triads at $h = -H$ (hence the value of A_3 does not impact the results shown). The frequency of the mode-1 wave is $\omega_3/N_b = 0.2$, while $f/\omega_3 = 0.4$ is taken. The stratification profile is given by:

(i) $N^{(8)}$: $N_{max} = 10N_b, W_p = H/50, z_c = H/20$.

Branch-1(2) triads have the higher (lower) frequency daughter wave propagating in the same direction as the parent wave. Figure 6 reveals that from both branches, the highest growth rates are centred around $n \approx m$. However, the majority of the white region contains resonant triads, but their growth rates are significantly lower in comparison to that clustered around $n \approx m$. Note that the central region is asymmetric between Branch-1 and Branch-2 triads, and this is purely a consequence of the internal wave's

dispersion relation. When the lower frequency daughter wave (wave-1) travels in the same direction as the parent wave (i.e. Branch-2), wave-1's mode number (n) should always be higher than wave-2's mode number (m) for the triad condition to be satisfied. However, for Branch-1, where wave-2 travels in the same direction as the parent wave, the mode number of wave-2 (n) need not be higher than wave-1's mode number (m).

The clustering around $n \approx m$ is observed consistently for any setting or stratification profile considered in our study. As a result, instead of focusing on all possible triads, we choose a specific line of interaction near the central region and plot the growth rate along that line of interaction. For example, the interaction lines (n, n) , $(n + 1, n)$ and $(n, n + 1)$ are plotted for $n \in (1, 50)$ in figures 7(a–c) for Branch-1 triads, and $(n + 4, n)$ in figure 7(d) for Branch-2 triads. The notation (a, b) means wave-1(2) is mode- $a(b)$. The notation is same for both branches. The dominant nature of the interaction lines (n, n) , $(n + 1, n)$ and $(n, n + 1)$ has also been observed in Young *et al.* (2008) while studying the stability of mode-1 internal waves in the presence of near inertial daughter waves (with frequency f). Furthermore, figure 7 also reveals that the different lines are sensitive to h . For completeness, we explore another stratification profile given by:

$$(i) N^{(9)}: N_{max} = 10N_b, W_p = H/50, z_c = H/80;$$

and the corresponding plots are in figure 8. Both figures 7 and 8 show that the growth rates along different lines of interaction have a significant oscillatory nature with n . In general, line (n, n) has the largest amplitude of oscillations. More importantly, the growth rate of a modal combination can change significantly as h changes. For example, figure 7(a) shows that the most unstable modal combination at $h = -H$ is $(5, 5)$. However, for $h = -0.8H$, the most unstable triad is the modal combination $(4, 4)$. Moreover, the combination $(5, 5)$ has approximately 0.25 times the $(4, 4)$ growth rate at $h = -0.8H$. This behaviour can be seen for the line (n, n) in both figures 7 and 8. This means effectively that the growth rate of certain daughter wave combinations can be sensitive to changes in h (especially the combinations that involve lower modes). Such combinations may not be effective in a region of varying h because of the significant drop in the growth rates. However, sensitivity to h is reduced slowly as the mode number is increased for both the branches. Even though Branch-2 triads have considerably lower growth rates for the profiles $N^{(8)}$ and $N^{(9)}$, for different profiles (not displayed here), Branch-2 can have σ comparable to that of the Branch-1 triads.

5.1.1. *Effect of variation of f/ω_3 and ω_3/N_b on different branches*

For both stratification profiles used in § 5.1, $f/\omega_3 = (0.3, 0.45)$ for $\omega_3/N_b = (0.2, 0.7)$ is explored (hence a total of four different combinations). For $N^{(8)}$, in all four cases, the qualitative behaviour of all Branch-1 lines is similar to figure 7. However, the maximum growth rate has a significant increase from $h = -H$ to $h = -0.8H$ for $\omega_3/N_b = 0.7$. Moreover, Branch-2 triads' maximum growth rate significantly increases in two cases of $f/\omega_3 = 0.3$ in comparison to $f/\omega_3 = 0.4$. For $N^{(9)}$, the qualitative behaviour of line (n, n) is similar to what was observed in $f/\omega_3 = 0.4$. In general, the maximum growth rate is the (n, n) modal combination. Interestingly, it is found that the maximum growth rate among all triads increased nearly twice from $h = -H$ to $h = -0.8H$ for $f/\omega_3 = 0.45$, $\omega_3/N_b = 0.7$. A significant increase in maximum growth rate is also found for $\omega_3/N_b = 0.2$ for the same f . For $f/\omega_3 = 0.3$, $\omega_3/N_b = 0.7$, the behaviour of line $(n + 1, n)$ has a significant oscillation with n , similar to line (n, n) . Note that this is different from the line

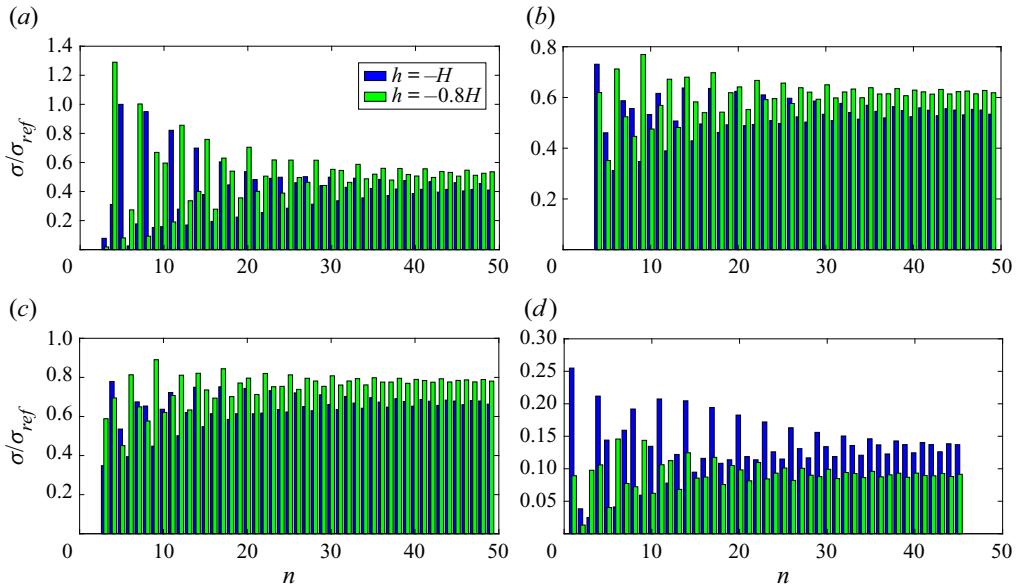


Figure 7. Plots of non-dimensional growth rates of mode-1 triads for profile $N^{(8)}$, with $f/\omega_3 = 0.4$ and $\omega_3/N_b = 0.2$: (a) line (n, n) of Branch-1; (b) line $(n + 1, n)$ of Branch-1; (c) line $(n, n + 1)$ of Branch-1; and (d) line $(n + 4, n)$ of Branch-2.

$(n + 1, n)$ shown in figure 8. In general, it is also observed that reducing the fluid depth increases the maximum growth rate of all possible triads even without considering the β term of the parent wave amplitude.

5.2. Variation of nonlinear coupling coefficient with domain height for self-interaction process

Here, we restrict to self-interaction of internal gravity waves that do not experience significant detuning $\Delta\mathcal{K}$ with changes in h . In this subsection, we focus mainly on the superharmonic wave’s nonlinear coupling coefficient \mathcal{N}_3 given in (2.30b).

5.2.1. Class-1 interactions

As mentioned previously in § 4.2, some Class-1 self-interactions can have negligible detuning even for a finite range of h/H . We study the variation of $\tilde{\mathcal{N}}_3$ under such circumstances; the different interactions considered (denoted by \mathcal{I}_p) are as follows:

$$\begin{aligned} \mathcal{I}_1 - [\text{P3,D2}] \quad \mathcal{I}_2 - [\text{P4,D2}] \quad \mathcal{I}_3 - [\text{P4,D3}] \quad \mathcal{I}_4 - [\text{P5,D3}] \quad \mathcal{I}_5 - [\text{P5,D4}] \\ \mathcal{I}_6 - [\text{P6,D3}] \quad \mathcal{I}_7 - [\text{P6,D4}] \quad \mathcal{I}_8 - [\text{P6,D5}] \quad \mathcal{I}_9 - [\text{P7,D4}] \quad \mathcal{I}_{10} - [\text{P7,D5}] \end{aligned}$$

Here, the notation $[\text{P}m,\text{D}n]$ denotes that the parent wave is the m th mode, and the daughter (superharmonic) wave is the n th mode.

The stratification profiles are chosen such that $N_{max} = (2N_b, 5N_b, 10N_b)$, $W_p = (H/200, H/100, H/50)$ and $z_c = (H/40, H/20, H/10)$. For the profiles considered, we study variations of $\tilde{\mathcal{N}}_3 \equiv |\mathcal{N}_3|/\max(|\mathcal{N}_3|)$ for interactions that strictly satisfy $|\Delta\mathcal{K}_s| < 0.01$ for $h/H \in [-1, -0.8]$. Figure 9 shows variations of $\tilde{\mathcal{N}}_3$ for two Class-1 self-interactions. Figure 9 reveals that interactions can have a non-monotonic variation

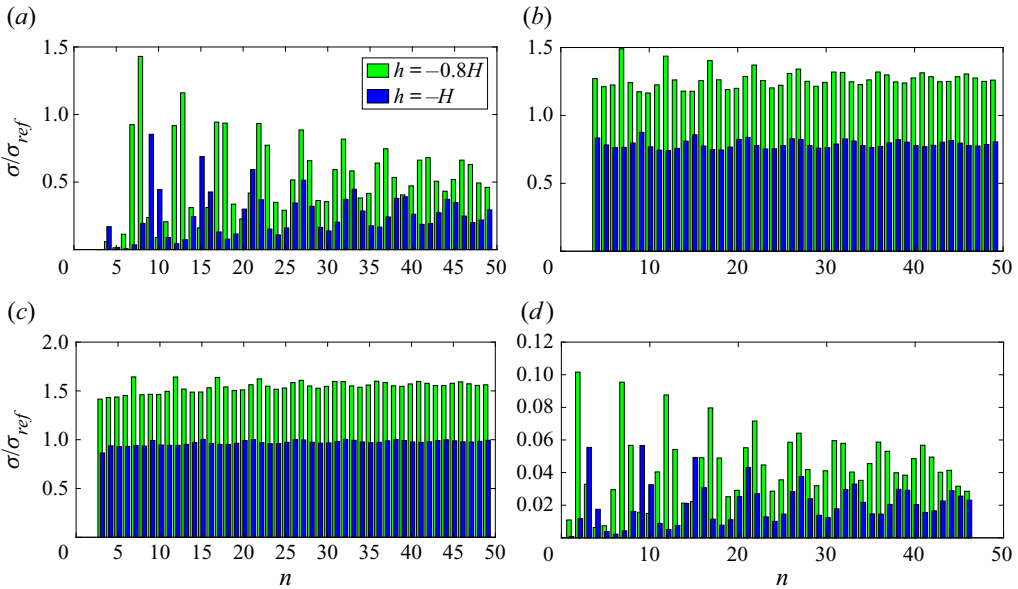


Figure 8. Plots of non-dimensional growth rates of mode-1 triads for profile $N^{(9)}$, with $f/\omega_3 = 0.4$ and $\omega_3/N_b = 0.2$: (a) line (n, n) of Branch-1; (b) line $(n + 1, n)$ of Branch-1; (c) line $(n, n + 1)$ of Branch-1; and (d) line $(n + 6, n)$ of Branch-2.

of $\tilde{\mathcal{N}}_3$ with h/H . Moreover, the figure reveals that even relatively small changes in h/H can lead to significant variations in $\tilde{\mathcal{N}}_3$. For all interactions \mathcal{I}_p considered in the list above, small changes in h/H can cause significant change in $\tilde{\mathcal{N}}_3$. Some generic features are summarized below. Sensitivity of $\tilde{\mathcal{N}}_3$ to h/H increases as z_c is increased for a given W_p, N_{max} . For every interaction, there are specific combinations of W_p, N_{max} where this behaviour is not exhibited. Moreover, increasing W_p also increases the sensitivity of $\tilde{\mathcal{N}}_3$ to changes in h/H . Increasing N_{max} for given (z_c, W_p) also increases the sensitivity of $\tilde{\mathcal{N}}_3$ to h/H .

5.2.2. Class-2 interactions

Initially, we study the variation of \mathcal{N}_3 with h for Class-2 self-interactions. To this end, we consider \mathcal{N}_3 of the first five modes for 27 different stratification profiles. Similar to the case of Class-1 self-interactions in § 5.2.1, the stratification profiles are chosen such that $N_{max} = (2N_b, 5N_b, 10N_b)$, $W_p = (H/200, H/100, H/50)$ and $z_c = (H/40, H/20, H/10)$, where we consider all possible (3^3) combinations. Out of the $3^3 = 27$ combinations, nine profiles are chosen for plotting in figure 10 and thereby elucidating the effect of each individual parameter in the stratification profile. For all cases, $\omega_3 = 0.1N_b$ and $f = 0$. For some higher modes, the nonlinear coupling coefficient has a band-like structure; there exists some range of h/H where $\tilde{\mathcal{N}}_3$ is significantly higher in magnitude than that corresponding to other values of h/H . For example, the mode $n = 5$ corresponding to $N_{max} = 5N_b$ in figure 10(c) reveals a large increase in $\tilde{\mathcal{N}}_3$ near $h/H \approx -0.75$, while it is much lower at either end. Wunsch (2017) also observed such a banded structure in the self-interaction of different modes as the stratification profile was changed. The reason behind the direct analogy between our observations and that of Wunsch (2017)

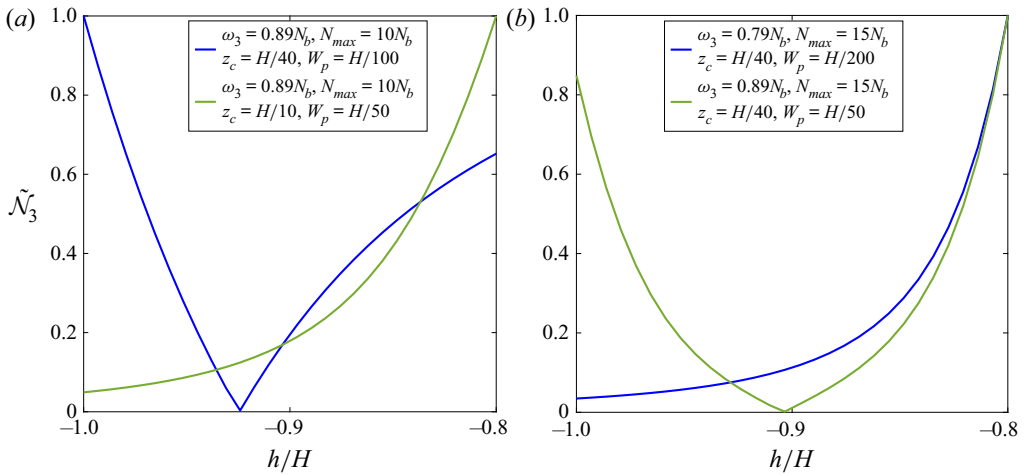


Figure 9. Variation of \tilde{N}_3 with h for Class-1 self-interactions: (a) \mathcal{I}_1 and (b) \mathcal{I}_{10} . Each panel shows plots for two different stratification profiles (for details, see legend).

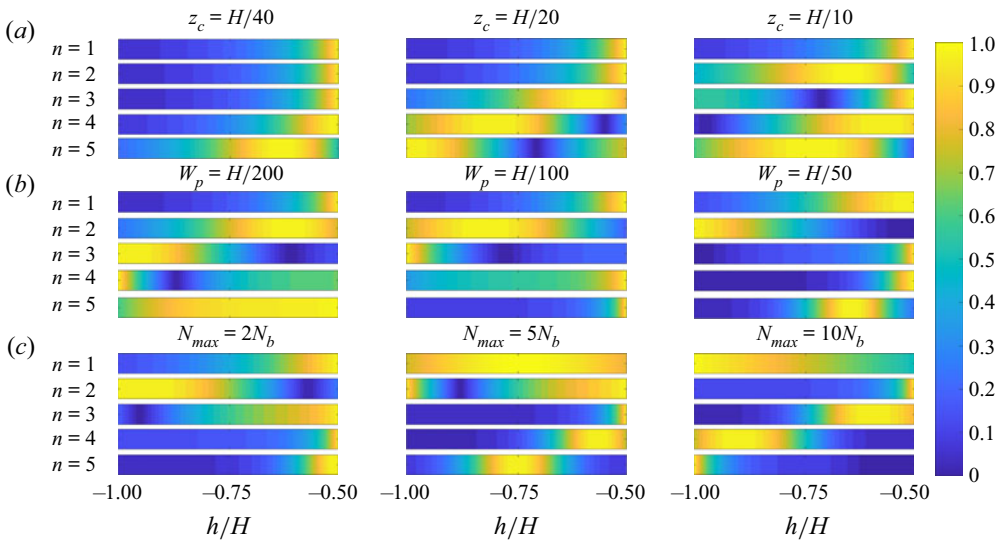


Figure 10. The variation of non-dimensionalized nonlinear coupling coefficient (\tilde{N}_3) of wave-3 (the superharmonic wave) as h is varied. Altogether, there are nine blocks, each consisting of five units, and each unit represents the mode number (given by n). For each block, (N_{max}, W_p, z_c) is fixed. The figure is further subdivided into three horizontal panels (each panel consisting of three blocks): (a) $N_{max} = 2N_b$, $W_p = H/200$, and z_c is varied; (b) $N_{max} = 5N_b$, $z_c = H/20$, and W_p is varied; and (c) $z_c = H/10$, $W_p = H/50$, and N_{max} is varied.

is straightforward – when an internal wave travels to a different domain height, essentially it travels to a different stratification profile.

For mode-1, when z_c, W_p, N_{max} are all on the lower side, we observe that $\tilde{N}_3 \propto 1/h^4$. For higher N_{max} , even lower values of z_c and W_p do not have the property $\tilde{N}_3 \propto 1/h^4$. In general for modes > 1 , proportionality to $1/h^4$ is lost faster as z_c, W_p, N_{max} are increased.

In several profiles, \tilde{N}_3 of higher modes is also more sensitive to changes in h than $\tilde{N}_3 \propto 1/h^4$.

6. Higher-order self-interactions in the presence of a small-amplitude monochromatic topography

The focus of this section is on higher-order self-interactions between a parent wave of frequency ω_1 and a superharmonic daughter wave of frequency $\omega_3 = 2\omega_1$ in the presence of a small-amplitude monochromatic topography. In such scenarios, the topography can act as a ‘zero frequency wave’, which can lead to resonant higher-order interactions, and is similar to the Class-2 studied in Alam *et al.* (2009) for surface gravity waves. Such higher-order self-interactions might be important for mode-1 internal waves propagating in regions where $f > \omega_d/2$ (where ω_d is the semidiurnal frequency), since triad interactions involving two (subharmonic) daughter waves is not possible. Moreover, resonant self-interaction for a mode-1 internal wave of frequency ω_d is also not possible when $f > \omega_d/2$ for any stratification profile, as a consequence of its dispersion relation (Wunsch 2017). This arises from the fact that a mode-1 parent wave with frequency ω_d and a superharmonic daughter wave with frequency $2\omega_d$ fail to satisfy the horizontal wavenumber condition for a self-interaction process. Note that higher-order interactions are different from Bragg resonance focused on in Buhler & Holmes-Cerfon (2011), which is also a mechanism via which a parent mode-1 wave can decay by transferring its energy to the higher modes. In a standard Bragg resonance, resonant wave–topography interaction occurs if the bottom topography has a wavenumber k_b such that $(\omega_1, k_b \pm k_1)$ satisfies the dispersion relation.

To study higher-order self-interactions, we follow the streamfunction ansatz used in Couston *et al.* (2017) for studying internal wave Bragg resonance, and in Lahaye & Llewellyn Smith (2020) for studying internal wave scattering due to interaction with a large-amplitude topography. This ansatz for the streamfunction of the j th wave is

$$\Psi_j = \mathcal{A}_j(x) \phi_j(\eta; x) e^{-i\omega_j t} + \text{c.c.} \tag{6.1}$$

The corresponding buoyancy frequency and meridional velocity are given by

$$B_j = \frac{iN^2}{\omega_j} \frac{\partial \mathcal{A}_j}{\partial x} \phi_j e^{-i\omega_j t} + \text{c.c.}, \tag{6.2}$$

$$\mathcal{V}_j = \frac{if}{\omega_j} \frac{\mathcal{A}_j}{h} \frac{\partial \phi_j}{\partial \eta} e^{-i\omega_j t} + \text{c.c.} \tag{6.3}$$

The above-mentioned ansatz can also be used to study systems where the detuning is $\Delta\mathcal{K}_s \sim O(1)$ in the presence of a flat or slowly varying bathymetry. The functions ϕ_j are same as the functions used in § 2 and are obtained by solving (2.13b). Here we consider only a small-amplitude topography whose wavenumber is comparable to the parent wave, i.e. $\epsilon_h \ll O(1)$ and $\epsilon_k \sim O(1)$.

To study higher-order interactions of a parent wave propagating in the presence of a small-amplitude topography, we also consider the linear scattering of the parent wave. Note that the linear scattering of the parent wave on its own is not resonant (we do not consider topography wavenumbers that allow resonant Bragg scattering) and hence over a long distance has a negligible effect on the parent wave’s amplitude. However, even

the non-resonant linear interaction of the parent wave with the topography, which leads to higher modes with ω_1 frequency, can impact significantly the growth of the superharmonic wave. To derive the linear scattering of the parent wave as it moves through a topography, we assume the streamfunction of the waves to be

$$\Psi_1 = \sum_{n=1}^{n=M_n} \mathcal{A}_{(1,n)}(x) \phi_{(1,n)}(\eta; x) e^{-i\omega_1 t} + \text{c.c.}, \tag{6.4}$$

where M_n is the maximum mode number after which the series is truncated, and $\phi_{(1,n)}$ is the n th eigenfunction of the ω_1 frequency. The streamfunction ansatz (6.4) is substituted in (2.5), and similar to § 2, the linear terms of (2.5) are multiplied by $\phi_{(1,n)}$ and integrated in the η direction. This leads to M_n ordinary differential equations, where the n th differential equation is given by

$$\begin{aligned} & \gamma_n^{(3)} \left[\frac{\partial^2 \mathcal{A}_{(1,n)}}{\partial x^2} + \mathcal{K}_{(1,n)}^2 \frac{\mathcal{A}_{(1,n)}}{h^2} \right] \\ &= - \sum_{m=1}^{m=M_n} \left[\frac{2\gamma_{(m,n)}^{(5)} + \gamma_{(m,n)}^{(6)}}{h^2} \left(\frac{\partial h}{\partial x} \right)^2 - \frac{2\gamma_{(m,n)}^{(7)}}{h} \frac{\partial h}{\partial x} \right] \mathcal{A}_{(1,m)} \\ & \quad - \sum_{m=1}^{m=M_n} \left[\gamma_{(m,n)}^{(8)} - \frac{\gamma_{(m,n)}^{(5)}}{h} \left(\frac{\partial^2 h}{\partial x^2} \right) \right] \mathcal{A}_{(1,m)} \\ & \quad - \sum_{m=1}^{m=M_n} 2 \left[\gamma_{(m,n)}^{(4)} - \frac{\gamma_{(m,n)}^{(5)}}{h} \frac{\partial h}{\partial x} \right] \frac{\partial \mathcal{A}_{(1,m)}}{\partial x}, \end{aligned} \tag{6.5}$$

where $\mathcal{K}_{(1,n)}$ is the corresponding eigenvalue of $\phi_{(1,n)}$. Moreover, $\gamma_{(m,n)}^{(*)}$ are evaluated using the expressions given in Appendix A. The above equations are similar to the equations derived in Lahaye & Llewellyn Smith (2020), except that we do not consider waves that travel in the direction opposite to the parent wave since they are assumed to be negligible. Now that we have the full wave spectrum with ω_1 frequency by solving (6.5), we model the evolution of the superharmonic wave. For simplicity, the feedback to the parent wave is neglected, which is analogous to the pump wave approximation used in § 2.

The streamfunction of the superharmonic wave Ψ_3 is substituted in (2.5), and the linear terms are multiplied by ϕ_3 and integrated in the η direction. This leads to

$$\begin{aligned} LIN_3 \equiv & \left[\left(\gamma_3^{(3)} \frac{\partial^2 \mathcal{A}_3}{\partial x^2} \right) + \mathcal{K}_3^2 \left(\frac{\mathcal{A}_3}{h^2} \gamma_3^{(3)} \right) \right] e^{-i\omega_3 t} \\ & + 2 \left[\frac{\gamma_3^{(5)}}{h^2} \left(\frac{\partial h}{\partial x} \right)^2 - \frac{\gamma_3^{(7)}}{h} \frac{\partial h}{\partial x} \right] \mathcal{A}_3 e^{-i\omega_3 t} \\ & + \left[\frac{\gamma_3^{(6)}}{h^2} \left(\frac{\partial h}{\partial x} \right)^2 - \frac{\gamma_3^{(5)}}{h} \left(\frac{\partial^2 h}{\partial x^2} \right) + \gamma_3^{(8)} \right] \mathcal{A}_3 e^{-i\omega_3 t} \\ & + 2 \left(\gamma_3^{(4)} - \frac{\gamma_3^{(5)}}{h} \frac{\partial h}{\partial x} \right) \frac{\partial \mathcal{A}_3}{\partial x} e^{-i\omega_3 t}, \end{aligned} \tag{6.6}$$

where LIN_3 contains only linear terms, and models the propagation of superharmonic wave in the presence of a topography. Note that a superharmonic wave cannot exchange energy with higher modes of ω_3 . Now we move on to deriving the nonlinear terms that force the superharmonic wave. Since we are focusing on higher-order interactions, all nonlinear terms (including terms containing x -direction derivatives of ϕ and h), which have the same angular frequency as the superharmonic wave, are retained. In the terrain-following coordinates, this would, however, lead to a large number of terms that need to be evaluated. This issue can be circumvented following the procedure outlined below. The nonlinear terms in the terrain-following coordinates are given by the right-hand side of (2.5).

We assume that the superharmonic wave is forced nonlinearly by the ω_1 spectrum. To model this, we substitute $\Psi_1, B_1, \mathcal{V}_1$ into the nonlinear terms of (2.5). Note that we can obtain B_1 and \mathcal{V}_1 from (6.2) and (6.3), respectively. After the substitution, similar to the linear terms of wave-3, the nonlinear terms are multiplied by ϕ_3 and integrated in the η -direction within the domain limits. The resultant expression obtained is

$$\langle NL_3 \rangle = \int_{-1}^0 \phi_3 [i\omega_3 \mathcal{J}\{(L_{xx} + L_{\eta\eta})\Psi_1, \Psi_1\} + L_x(\mathcal{J}\{B_1, \Psi_1\}) - f L_\eta(\mathcal{J}\{\mathcal{V}_1, \Psi_1\})] d\eta. \tag{6.7}$$

Therefore the final superharmonic wave equation can be written in a compact form:

$$LIN_3 = \langle NL_3 \rangle. \tag{6.8}$$

In (6.6) and (6.8), instead of splitting \mathcal{A}_j into a product of slowly varying amplitude and rapidly varying phase part, we simply solve the equations numerically by retaining \mathcal{A}_j as it is. This is mainly because, as mentioned above, the number of nonlinear terms would be significantly high in terrain-following coordinates. For high ratios of f/ω_1 (for example, north of the critical latitude), the parent wave cannot self-interact resonantly with the superharmonic wave in the presence of a flat bottom. However, a resonant higher-order self-interaction can occur provided that the topography has a wavenumber k_b such that

$$k_b = k_3 - 2k_1, \tag{6.9}$$

where k_3 is the wavenumber of the superharmonic wave, and the k_1 is the wavenumber of the parent wave. In such scenarios, the daughter wave's amplitude will grow consistently. However, this being a higher-order interaction, the growth rate of the daughter wave (consequently, the decay of the parent wave) can be expected to be slower than a resonant self-interaction.

To elucidate and validate the higher-order self-interaction process, we perform numerical simulations by solving the complete 2-D Boussinesq equations and comparing the output with the results of the reduced-order model derived in this section. We run three simulations where the parent and daughter waves' frequencies are held fixed. They are denoted by Case-1, Case-2 and Case-3. For all the simulations, the parent wave frequency is $\omega_1/N_b = 0.2$, where ω_1 is the semi-diurnal frequency, i.e. $\omega_1 = 1.4 \times 10^{-4} \text{ s}^{-1}$. Both the parent and daughter waves are mode-1 of their respective frequencies (ω_1 and $2\omega_1$). These parameters would result in a significant detuning between the two waves at high f values. The bathymetry profile is given by

$$h = -H + [\epsilon_h H \sin(k_b(x - x_c))] \times \frac{1}{1 + (x - x_c)^{32}/W_T^{32}}, \tag{6.10}$$

where $\epsilon_h = 0.01$, $H = 3000 \text{ m}$, and domain length $L = 540H$ and $x_c = L/2$ are held fixed across all three simulations. The stratification profile parameters, f value, incoming

	W_p/H	z_c/H	N_{max}/N_b	f/ω_d	u_{max} (m s ⁻¹)	W_T/L
Case-1	1/16	1.5/1000	4.5	0.58	0.0120	0.30
Case-2	29.5/400	1.5/1000	7	0.64	0.0227	0.30
Case-3	1/20	1.5/1000	10	0.60	0.0232	0.31

Table 1. The stratification profile parameters, Coriolis frequency W_T , and velocity amplitude of the three waves for Case-1, Case-2 and Case-3.

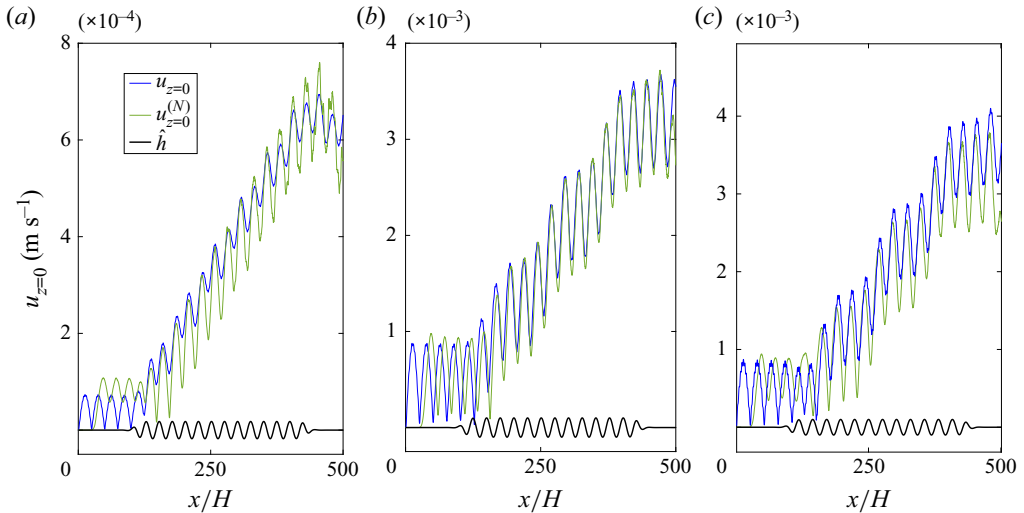


Figure 11. Higher-order self-interaction of mode-1 internal waves in the presence of a monochromatic bathymetry for three different cases: (a) Case-1, (b) Case-2, and (c) Case-3. The topography profile (not to scale) is shown for all three cases.

maximum velocity of the parent mode (u_{max}), and W_T for the three simulations are given in table 1.

The results after solving the reduced-order model and 2-D Boussinesq equations for the above-mentioned parameters are shown in figure 11. The 2-D Boussinesq equations are solved using Dedalus (Burns *et al.* 2020). More details on the simulations are given at the end of § 7. In figures 11(a–c), the amplitude of the daughter wave is observed to be slowly increasing due to the higher-order self-interaction. Moreover, the daughter wave’s amplitude also rapidly oscillates because of the non-resonant standard self-interaction process between the parent wave and the daughter wave. In the absence of a varying bathymetry, only the rapid non-resonant interaction would be present without any consistent growth in the daughter wave’s amplitude. Therefore, we have shown that for scenarios where Bragg resonances are not resonant, higher-order interaction might be a possible mechanism that can scatter the energy of the mode-1 internal wave.

7. Numerical validation

In this section, we provide numerical validations for the reduced-order equations (2.29a) and (2.29b) derived through multiple-scale analysis for two different cases. This is done by solving the 2-D Boussinesq equations in terrain-following coordinates using the

open-source, pseudo-spectral code Dedalus (Burns *et al.* 2020). The above-mentioned equations in primitive variables along with viscous and hyperviscous terms (the latter terms damping much smaller scales than the former) are

$$\frac{\partial u}{\partial t} + L_x(P) + uL_x(u) + wL_\eta(u) = \nu L_{\eta\eta}(u) + \left(\frac{\nu_{6z}}{H^6} \frac{\partial^6 u}{\partial \eta^6} + \nu_{6x} \frac{\partial^6 u}{\partial x^6} \right), \quad (7.1a)$$

$$\frac{\partial w}{\partial t} + L_\eta(P) + uL_x(w) + wL_\eta(w) = \nu L_{\eta\eta}(w) + B, \quad (7.1b)$$

$$\frac{\partial B}{\partial t} + N^2 w + uL_x(B) + wL_\eta(B) = \nu L_{\eta\eta}(B) + \left(\frac{\nu_{6z}}{H^6} \frac{\partial^6 B}{\partial \eta^6} + \nu_{6x} \frac{\partial^6 B}{\partial x^6} \right), \quad (7.1c)$$

$$L_x(u) + L_\eta(w) = 0. \quad (7.1d)$$

Here, $(u, w) = (L_\eta(\Psi), -L_x(\Psi))$, meaning that here the velocity field is defined in x - η instead of x - z coordinates. In all our simulations, $\nu = 10^{-5} \text{ m}^2 \text{ s}^{-1}$, $\nu_{6x} = 10^8 \text{ m}^6 \text{ s}^{-1}$ and $\nu_{6z} = 81 \text{ m}^6 \text{ s}^{-1}$. Equations (2.29a) and (2.29b) are solved using the fourth-order Runge Kutta method for time stepping and a second-order-accurate discretization scheme for the term $\partial a_i / \partial x$, where the scheme is forward or backward depending on the group speed direction of the particular wave. We estimate the validity of two different cases.

For Case-1, self-interaction of a plane wave in the presence of a constant h is simulated. The parameters of the simulation are $H = 3000 \text{ m}$ and $N_b = 10^{-3} \text{ s}^{-1}$. The frequency of the parent wave is taken as $\omega_1/N_b = 0.447$, while $f = 0$ is chosen. The stratification profile (4.1) is considered, and the parameters used are:

- (i) $N^{(13)}$: $N_{max} = 3N_b$, $W_p = 3H/100$, $z_c = H/10$.

Mode-3 of the parent wave frequency (ω_1) in this scenario self-interacts resonantly with mode-2 of $2\omega_1$ (Varma & Mathur 2017). The parent wave streamfunction input (initial condition) to the full numerical simulation is given by

$$\Psi = A_1 \phi_1 \sin(k_1 x) \exp(-(x - x_c)^2 / W_1^2), \quad (7.2)$$

where $|A_1| = 0.06$, $W_1 \rightarrow \infty$ is chosen (note that x_c can be any value since $W_1 \rightarrow \infty$), and Ψ is used to obtain (u, w) . The numerical code is also initialized with the corresponding buoyancy frequency for the streamfunction given in (7.2).

For estimating the energy of parent and daughter waves from the numerical simulations, only the potential energy of the waves is considered. This is valid because when $f = 0$, energy is partitioned equally between potential energy and kinetic energy. For evaluating the potential energy of the two waves, we take the Fourier transform of B in the x -direction. Then by simply isolating the k_3 and k_1 wavenumbers, the respective fields due to wave-3 and wave-1 can be obtained for all time. The resulting energy evolution of the waves for Case-1 is shown in figure 12(a). At the end of the simulation, the parent wave energy was observed to be 86% of the total energy in the Boussinesq equations simulation, while the reduced-order model predicted that 85.5% of the total energy will be contained in the parent wave at the specified time interval. Moreover, at the end of the simulation, the daughter wave's energies in the Boussinesq equations simulation and the reduced-order model are 13.0% and 14.4%, respectively.

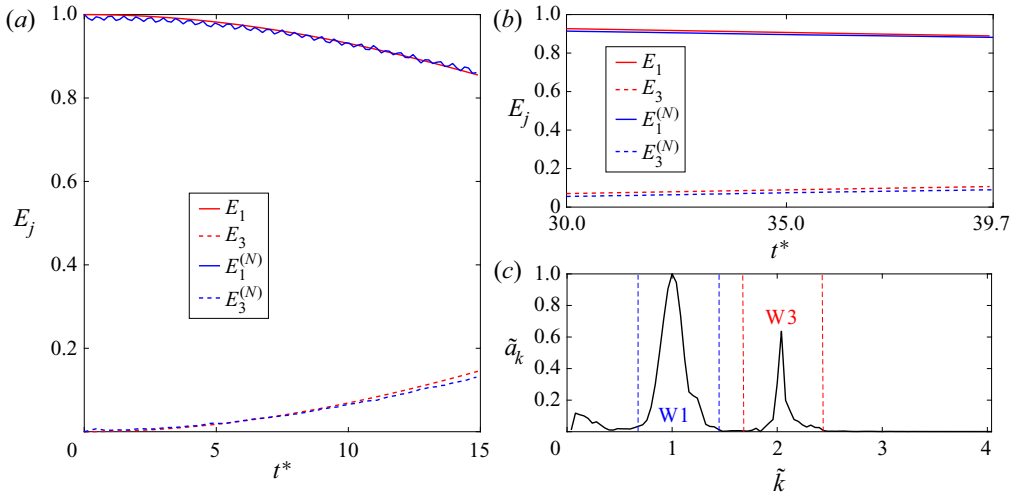


Figure 12. (a) The energy evolution of waves for Case-1 from reduced-order equations and numerical simulations. The superscript (N) denotes the results from numerical simulation of 2-D Boussinesq equations. (b) The energy evolution of waves for Case-2 from reduced-order equations and numerical simulations in the time span $t^* = 30$ to $t^* \approx 40$, where $t^* \equiv \omega_1 t / 2\pi$. (c) Fourier transform of B at $\eta = -0.42$ and $t^* = 40$. Here, W1 and W3 indicate wave-1 and wave-3, respectively.

In Case-2, we consider the self-interaction of a parent wave packet travelling in the presence of a slowly varying bathymetry. The parameters considered are $H = 3000$ m and $N_b = 2.5 \times 10^{-3} \text{ s}^{-1}$. The following stratification profile is used:

(i) $N^{(14)}$: $N_{max} = 5N_b$, $W_p = 3H/100$, $z_c = H/10$.

Here, $\omega_1/N_b = 0.447$ with $f = 0$ are chosen. Mode-3 of ω_1 self-interacts resonantly with mode-2 of $2\omega_1$ for $h/H \in [-1, -0.8]$. The bathymetry is given by

$$h = -H + 0.1H \left[\tanh((x - x_{t1})/W_{t1}) + \tanh((x_{t2} - x)/W_{t2}) \right], \tag{7.3}$$

where $W_{t1} = 2.7H$, $W_{t2} = W_{t1}/1.3$, $x_{t1} = 25H$ and $x_{t2} = 83H$ were considered, where $100H$ is the domain length in the x -direction. The bathymetry shape can be visualized in figure 13.

The parent wave streamfunction of the form (7.2) is used with $|A_1| = 0.022$, $W_1 = 3.57H$, and $x_c = 10.2H$ is chosen. Here, k_1 is evaluated at $h = -H$ for the initial conditions. The x_c value is chosen such that the wave packet is just at the bottom of the ‘plateau-like’ topography at $t = 0$ (as shown in figure 13a). The bathymetry is considered to be slowly varying so that the wave packet scattering by the bathymetry is negligible. Here, the same procedure of energy evaluation as for Case-1 is followed, except that the energy is evaluated from $t^* = 30$, when the entire energy of both wave packets is almost confined to the top of the plateau region (where $h = -0.8H$). This makes the energy evaluation straightforward. We consider B only in the range $x/H \in [33, 68]$ (where most of the energy is contained), and then again perform a Fourier transform to separate the energy of the daughter and parent wave packets.

In Case-2, since wave packets are considered, the Fourier transform of B would not have a sharp peak at k_1 and k_3 . Instead, a smoother peak in k -space would be produced as shown in figure 12(c). We define a non-dimensional wavenumber \tilde{k} as $\tilde{k} \equiv k/k_1$. For evaluating

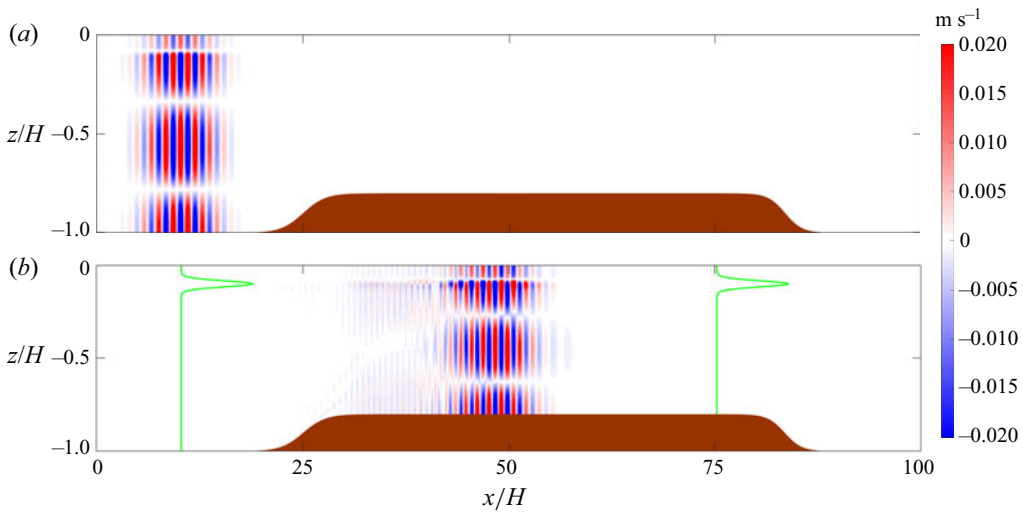


Figure 13. Horizontal velocity plot (u) from Case-2 simulation at (a) $t^* = 0$ and (b) $t^* = 30$. The stratification profile shape used is also shown for visual purposes. A faint but clear mode-2 trail left by the mode-3 parent wave can be seen in (b). The shape of the stratification profile used in Case-2 is given by green curves in (b).

the energy of both wave packets, amplitude ($|a_{\tilde{k}}|$) in a finite range of \tilde{k} is considered. The energy contained in $\tilde{k} \in [0.6, 1.4]$ is considered as the energy of the parent wave packet, while the energy in $\tilde{k} \in [1.6, 2.4]$ is considered as the daughter wave's energy. For example, the \tilde{k} ranges considered for the parent and daughter waves are highlighted in figure 12(c) using coloured dashed lines for a specific η and t^* . For the parent wave, $|a_{\tilde{k}}|$ between the blue dashed lines is considered. Similarly, for evaluating the energy of the daughter wave packet, we consider the amplitude $|a_{\tilde{k}}|$ between the red dashed lines. The energy evolution of the wave packets is shown in figure 12(b). The parent wave packet energies in the Boussinesq equations simulation and the reduced-order model were observed to be 88.1% and 88.9%, respectively, at the end of the simulations. At the same time, the daughter wave's energies in the Boussinesq equations simulation and the reduced-order model are 8.95% and 10.6%, respectively.

To obtain the numerical results in figure 11, (7.1a)–(7.1d) along with the equation for meridional velocity (v) were solved. A vertical hyperviscous term was not used, while a different horizontal hyperviscous term was used: $\nu_{12x} \partial^{12} / \partial x^{12}$, where $\nu_{12x} = 1.4 \times 10^{25} \text{ m}^2 \text{ s}^{-1}$. The kinematic viscosity was chosen to be $\nu = 10^{-3} \text{ m}^2 \text{ s}^{-1}$. The primary wave was forced by using a forcing function in the u -momentum equation, which sends a constant-amplitude mode-1 wave train onto the small-amplitude topography.

8. Summary and conclusion

Weakly nonlinear wave–wave interactions is one of the mechanisms through which internal gravity waves energy cascade from large length scales (hundreds of kilometres) to small scales (centimetres to metres). At small length scales, internal waves can give rise to convective or shear instabilities (Koudella & Staquet 2006) and cause mixing, thus resulting in increased diffusion in oceans. The 2-D Boussinesq equations are

written in terrain-following coordinates ($x-\eta$). Using multiple-scale analysis, we derive the amplitude evolution equations for internal gravity waves undergoing weakly nonlinear wave-wave interactions in the presence of varying density stratification (resembling that of actual oceanic scenarios) as well as mild-slope bathymetry in a vertically bounded domain. If the stratification varies with z in the $x-z$ coordinates, then it becomes a function of both x and η in the $x-\eta$ coordinates when bathymetry h varies with x . In other words, the effective stratification profile varies with the ocean depth. Both triads and self-interactions are studied, and both pure resonant conditions as well as systems with wavenumber detuning are analysed. The main results of this paper are given in a brief format in [figure 14](#).

In the presence of uniform stratification, we show that the horizontal wavenumber triad condition, given by $k_{(1,a)} + k_{(2,b)} + k_{(3,c)} = 0$, is not violated due to changes in h . Here, a, b, c are the mode numbers of waves 1, 2 and 3, respectively. Moreover, in the presence of uniform stratification, the nonlinear coupling coefficients are inversely proportional to the square of the fluid depth ($\propto 1/h^2$).

For non-uniform stratifications, we define two classes of interaction for both triads and self-interactions. Class-1 involves weakly nonlinear interactions of waves that do not have the same mode number. Class-2 is a special situation that involves interactions of waves with the same mode number, i.e. $a = b = c$. Class-2 triad interactions can exist only in the parameter regime $f \ll \omega_j \ll N$. Moreover, in the same parameter regime, near-resonant Class-2 self-interactions can exist with very low detuning even as h is varied. This is because the wavenumbers involved in a self-interaction change in the same way as h changes. For Class-1 interactions, detuning may be induced in triads and self-interactions if the waves interact in a region of varying h . This is because in a vertically bounded domain, the horizontal wavenumbers are not only a function of h but also a function of the mode number. Moreover, the functional dependence of the wavenumber on h may change as the mode number changes. Therefore, in a weakly nonlinear interaction where different mode numbers are involved, there is no constraint for the wavenumbers to satisfy the triad condition in a given range of h .

The variation of the growth rate of the daughter waves in both triadic- and self-interactions is studied when h is varied. For both Class-1 and Class-2 self-interactions, it is observed that small changes in h may result in large changes in the growth rate of the daughter waves. This characteristic is observed especially for Class-1 self-interactions. Variation of growth rates with h is studied for triads of a mode-1 parent wave in the presence of non-uniform stratification. Triads were identified such that the daughter waves can be up to mode-50. For relatively small changes in h , the growth rates can vary significantly for triads that involve only lower modes. Moreover, the most unstable daughter wave combination for the same parent wave can also change for relatively small changes in h . Unlike uniform stratification, in non-uniform stratification, the growth rates do not have a monotonic behaviour with h . This was observed for both triadic- and self-interactions.

Reduced-order equations for higher-order self-interactions of an internal wave in the presence of a small-amplitude monochromatic topography are also derived. In the higher-order self-interaction process, the small-amplitude topography behaves as a zero-frequency wave. It is shown that such higher-order interactions can cause resonant growth of the superharmonic wave. Such higher-order interactions can play a crucial role in the decay of the mode-1 internal wave at latitudes greater than 28.9° . This is because sum-type triad interactions are not possible (Olbers, Pollmann & Eden 2020), and a mode-1 internal wave cannot self-interact resonantly for high values of f (Wunsch 2017).

Non-uniform stratification		Uniform stratification
Class-1	<ul style="list-style-type: none"> ➤ Resonant interactions are possible for any ω_j. ➤ Nonlinear coefficients may increase or decrease with h. ➤ Interaction can get detuned as h is varied. ➤ Growth rates can be sensitive to change in h. 	<ul style="list-style-type: none"> ➤ Nonlinear coefficients are $\propto 1/h^2$. ➤ Detuning does not change with h.
Class-2	<ul style="list-style-type: none"> ➤ Resonant interactions are possible only for $f \ll \omega_j \ll N$. ➤ Nonlinear coefficient may increase or decrease with h. ➤ Detuning will be small even with $O(1)$ variation in h. 	<ul style="list-style-type: none"> ➤ Class-2 interactions are not possible.
Higher-order self-interactions	<ul style="list-style-type: none"> ➤ Topography behaves as a zero-frequency wave. ➤ Occurs when $k_b = k_3 - 2k_1$. ➤ Superharmonic wave grows linearly with x. ➤ Parent wave non-resonant interaction with topography can increase the superharmonic wave growth. 	

Figure 14. A summary diagram shows how different factors such as detuning and nonlinear coefficients can vary for different classes of interaction in the presence of non-uniform stratification. It also provides a brief picture of the higher-order self-interaction studied in § 6.

Declaration of interests. The authors report no conflict of interest.

Author ORCIDs.

- Saranraj Gururaj <https://orcid.org/0000-0001-6446-4005>;
- Anirban Guha <https://orcid.org/0000-0002-1368-6131>.

Appendix A. Expressions for γ_j , Γ_j and $NL_{(*,j)}$

The expressions for $\gamma_{(j,i)}^{(n)}$, which are used in §§ 2.2.1 and 6, are as follows:

$$\left. \begin{aligned}
 \gamma_{(j,i)}^{(1)} &= \int_{-1}^0 [\phi_j] \phi_i \, d\eta, & \gamma_{(j,i)}^{(2)} &= \int_{-1}^0 \left[\frac{\partial^2 \phi_j}{\partial \eta^2} \right] \phi_i \, d\eta, \\
 \gamma_{(j,i)}^{(3)} &= \int_{-1}^0 [(N^2 - \omega_j^2) \phi_j] \phi_i \, d\eta, & \gamma_{(j,i)}^{(4)} &= \int_{-1}^0 \left[(N^2 - \omega_j^2) \frac{\partial \phi_j}{\partial x} \right] \phi_i \, d\eta, \\
 \gamma_{(j,i)}^{(5)} &= \int_{-1}^0 \left[\eta (N^2 - \omega_j^2) \frac{\partial \phi_j}{\partial \eta} \right] \phi_i \, d\eta, & \gamma_{(j,i)}^{(6)} &= \int_{-1}^0 \left[\eta^2 (N^2 - \omega_j^2) \frac{\partial^2 \phi_j}{\partial \eta^2} \right] \phi_i \, d\eta, \\
 \gamma_{(j,i)}^{(7)} &= \int_{-1}^0 \left[\eta (N^2 - \omega_j^2) \frac{\partial^2 \phi_j}{\partial x \partial \eta} \right] \phi_i \, d\eta, & \gamma_{(j,i)}^{(8)} &= \int_{-1}^0 \left[(N^2 - \omega_j^2) \frac{\partial^2 \phi_j}{\partial x^2} \right] \phi_i \, d\eta.
 \end{aligned} \right\} \tag{A1}$$

Throughout the paper, $\gamma_{(j,i)}$ is simply denoted by γ_j for convenience.

The expressions for $NL_{(*,j)}$ used in amplitude evolution equations (2.24a)–(2.24c) in § 2.2.1 are provided below (note that $NL_{(*,j)}$ is used in (2.25b)):

$$\left. \begin{aligned}
 NL_{(\psi,1)} &= \frac{\omega_1}{h^4} \left[\mathcal{K}_3 \left(\zeta_3 \omega_3^2 \Gamma_2^{(1)} - \zeta_3 \Gamma_2^{(2)} - \Gamma_3^{(3)} \right) - \mathcal{K}_2 \left(\zeta_2 \omega_2^2 \Gamma_3^{(1)} - \zeta_2 \Gamma_3^{(2)} - \Gamma_2^{(3)} \right) \right] \\
 &\quad + \frac{\omega_1}{h^4} \left[\left(\mathcal{K}_2^2 - \mathcal{K}_3^2 \right) \left(\mathcal{K}_2 \Gamma_3^{(1)} + \mathcal{K}_3 \Gamma_2^{(1)} \right) \right], \\
 NL_{(\psi,2)} &= \frac{\omega_2}{h^4} \left[\mathcal{K}_3 \left(\zeta_3 \omega_3^2 \Gamma_1^{(1)} - \zeta_3 \Gamma_1^{(2)} - \Gamma_3^{(3)} \right) - \mathcal{K}_1 \left(\zeta_1 \omega_1^2 \Gamma_3^{(1)} - \zeta_1 \Gamma_3^{(2)} - \Gamma_1^{(3)} \right) \right] \\
 &\quad + \frac{\omega_2}{h^4} \left[\left(\mathcal{K}_1^2 - \mathcal{K}_3^2 \right) \left(\mathcal{K}_1 \Gamma_3^{(1)} + \mathcal{K}_3 \Gamma_1^{(1)} \right) \right], \\
 NL_{(\psi,3)} &= \frac{\omega_3}{h^4} \left[\mathcal{K}_1 \left(\zeta_2 \omega_2^2 \Gamma_1^{(1)} - \zeta_2 \Gamma_1^{(2)} - \Gamma_2^{(3)} \right) + \mathcal{K}_2 \left(\zeta_1 \omega_1^2 \Gamma_2^{(1)} - \zeta_1 \Gamma_2^{(2)} - \Gamma_1^{(3)} \right) \right] \\
 &\quad + \frac{\omega_3}{h^4} \left[\left(\mathcal{K}_2^2 - \mathcal{K}_1^2 \right) \left(\mathcal{K}_1 \Gamma_2^{(1)} - \mathcal{K}_2 \Gamma_1^{(1)} \right) \right];
 \end{aligned} \right\} \tag{A2}$$

$$\left. \begin{aligned}
 NL_{(B,1)} &= \frac{(\mathcal{K}_3 - \mathcal{K}_2)}{h^4} \left[\mathcal{K}_2 \mathcal{K}_3 \left(\frac{1}{\omega_2} - \frac{1}{\omega_3} \right) \Gamma^{(4)} \right] \\
 &\quad + \left(\frac{\mathcal{K}_3}{\omega_3} - \frac{\mathcal{K}_2}{\omega_2} \right) \left(\mathcal{K}_3 \Gamma_2^{(2)} - \mathcal{K}_2 \Gamma_3^{(2)} \right), \\
 NL_{(B,2)} &= \frac{(\mathcal{K}_3 - \mathcal{K}_1)}{h^4} \left[\mathcal{K}_1 \mathcal{K}_3 \left(\frac{1}{\omega_1} - \frac{1}{\omega_3} \right) \Gamma^{(4)} \right] \\
 &\quad + \left(\frac{\mathcal{K}_3}{\omega_3} - \frac{\mathcal{K}_1}{\omega_1} \right) \left(\mathcal{K}_3 \Gamma_1^{(2)} - \mathcal{K}_1 \Gamma_3^{(2)} \right), \\
 NL_{(B,3)} &= \frac{(\mathcal{K}_1 + \mathcal{K}_2)}{h^4} \left[\mathcal{K}_1 \mathcal{K}_2 \left(\frac{1}{\omega_1} + \frac{1}{\omega_2} \right) \Gamma^{(4)} \right] \\
 &\quad + \left(\frac{\mathcal{K}_2}{\omega_2} - \frac{\mathcal{K}_1}{\omega_1} \right) \left(\mathcal{K}_1 \Gamma_2^{(2)} - \mathcal{K}_2 \Gamma_1^{(2)} \right);
 \end{aligned} \right\} \tag{A3}$$

$$\left. \begin{aligned}
 NL_{(\nu,1)} &= \frac{f^2}{h^4} \left[\left(\frac{1}{\omega_3} + \frac{1}{\omega_2} \right) \left(\mathcal{K}_2 + \mathcal{K}_3 \right) \left(\zeta_3 \omega_3^2 \Gamma_2^{(1)} - \zeta_3 \Gamma_2^{(2)} + \zeta_2 \omega_2^2 \Gamma_3^{(1)} - \zeta_2 \Gamma_3^{(2)} \right) \right] \\
 &\quad + \frac{f^2}{h^4} \left[\left(\frac{\mathcal{K}_2}{\omega_3} + \frac{\mathcal{K}_3}{\omega_2} \right) \left(\Gamma_2^{(3)} + \Gamma_3^{(3)} \right) \right], \\
 NL_{(\nu,2)} &= \frac{f^2}{h^4} \left[\left(\frac{1}{\omega_3} + \frac{1}{\omega_1} \right) \left(\mathcal{K}_1 + \mathcal{K}_3 \right) \left(\zeta_3 \omega_3^2 \Gamma_1^{(1)} - \zeta_3 \Gamma_1^{(2)} + \zeta_1 \omega_1^2 \Gamma_3^{(1)} - \zeta_1 \Gamma_3^{(2)} \right) \right] \\
 &\quad + \frac{f^2}{h^4} \left[\left(\frac{\mathcal{K}_1}{\omega_3} + \frac{\mathcal{K}_3}{\omega_1} \right) \left(\Gamma_1^{(3)} + \Gamma_3^{(3)} \right) \right], \\
 NL_{(\nu,3)} &= \frac{f^2}{h^4} \left[\left(\frac{1}{\omega_1} - \frac{1}{\omega_2} \right) \left(\mathcal{K}_1 - \mathcal{K}_2 \right) \left(\zeta_1 \omega_1^2 \Gamma_2^{(1)} - \zeta_1 \Gamma_2^{(2)} + \zeta_2 \omega_2^2 \Gamma_1^{(1)} - \zeta_2 \Gamma_1^{(2)} \right) \right] \\
 &\quad - \frac{f^2}{h^4} \left[\left(\frac{\mathcal{K}_2}{\omega_1} + \frac{\mathcal{K}_1}{\omega_2} \right) \left(\Gamma_2^{(3)} + \Gamma_1^{(3)} \right) \right].
 \end{aligned} \right\} \tag{A4}$$

Moreover, the $\Gamma_j^{(n)}$ are defined as follows:

$$\left. \begin{aligned}
 \Gamma_1^{(1)} &= \int_{-1}^0 \phi_2 \phi_3 \frac{\partial \phi_1}{\partial \eta} d\eta, & \Gamma_2^{(1)} &= \int_{-1}^0 \phi_1 \phi_3 \frac{\partial \phi_2}{\partial \eta} d\eta, \\
 \Gamma_3^{(1)} &= \int_{-1}^0 \phi_2 \phi_1 \frac{\partial \phi_3}{\partial \eta} d\eta, \\
 \Gamma_1^{(2)} &= \int_{-1}^0 N^2 \phi_2 \phi_3 \frac{\partial \phi_1}{\partial \eta} d\eta, & \Gamma_2^{(2)} &= \int_{-1}^0 N^2 \phi_1 \phi_3 \frac{\partial \phi_2}{\partial \eta} d\eta, \\
 \Gamma_3^{(2)} &= \int_{-1}^0 N^2 \phi_2 \phi_1 \frac{\partial \phi_3}{\partial \eta} d\eta, \\
 \Gamma_1^{(3)} &= \int_{-1}^0 \phi_2 \phi_3 \frac{\partial^3 \phi_1}{\partial \eta^3} d\eta, & \Gamma_2^{(3)} &= \int_{-1}^0 \phi_1 \phi_3 \frac{\partial^3 \phi_2}{\partial \eta^3} d\eta, \\
 \Gamma_3^{(3)} &= \int_{-1}^0 \phi_2 \phi_1 \frac{\partial^3 \phi_3}{\partial \eta^3} d\eta, \\
 \Gamma^{(4)} &= \int_{-1}^0 \frac{\partial N^2}{\partial \eta} \phi_1 \phi_2 \phi_3 d\eta.
 \end{aligned} \right\} \quad (A5)$$

Appendix B. Scaling analysis for finding the relation between the small parameters

Here we perform a scaling analysis for all the terms appearing in (2.21). Equation (2.21) is chosen here so that scaling analysis can be also done for the different terms that compose the β_j function in (2.22). Integrals γ_j in (2.21) (where γ_j expressions are given in (A1)) cannot be simplified analytically for non-uniform stratification profiles. Hence we adopt a numerical approach where we study how different integrals scale in an ensemble of stratification profiles that resemble the profiles used throughout the paper. Using this information, we scale the different terms. To this end, the stratification profiles are chosen such that $N_{max} = (5N_b, 10N_b, 15N_b)$, $W_p = (H/100, 2H/100, 3H/100)$ and $z_c = (H/80, H/40, H/20, H/10)$; and we consider all possible (36) combinations.

The analysis provides a relation between the time scale of the amplitude’s temporal evolution ($\epsilon_t t$), the length scale of the amplitude function ($\epsilon_x x$), and the magnitude of the waves’ amplitude ($\epsilon_a a_j$). Small parameters ϵ_h, ϵ_k represent the bathymetry, and they also influence the wave amplitude evolution. Equation (2.21), after some simplifications to the nonlinear term, is

$$\begin{aligned}
 \frac{\partial a_j}{\partial t} + \frac{1}{\mathfrak{D}_j} & \left[2i\gamma_j^{(3)} \left(\frac{\mathcal{K}_j}{h} \frac{\partial a_j}{\partial x} \right) + \frac{\gamma_j^{(6)}}{h^2} \left(\frac{dh}{dx} \right)^2 a_j \right] \\
 + \frac{1}{\mathfrak{D}_j} & \left[\frac{2\mathcal{K}_j}{h} \gamma_j^{(4)} + \gamma_j^{(3)} \frac{\partial}{\partial x} \left(\frac{\mathcal{K}_j}{h} \right) - \gamma_j^{(5)} \frac{2}{h} \frac{\partial h}{\partial x} \left(\frac{\mathcal{K}_j}{h} \right) - \frac{\gamma_j^{(3)}}{\beta_j} \frac{2\mathcal{K}_j}{h} \frac{d\beta_j}{dx} \right] a_j = \widehat{\mathfrak{N}}_j a^2,
 \end{aligned} \quad (B1)$$

where $\widehat{\mathfrak{N}}_j$ is defined as

$$\widehat{\mathfrak{N}}_j = \frac{1}{\mathfrak{D}_j} [NL_{(\mathcal{V},j)} + NL_{(B,j)} + NL_{(\psi,j)}]. \quad (B2)$$

The analysis is similar for all three waves, hence from here on all subscripts j (denoting the j th wave) are dropped for convenience. Moreover, a term containing $\gamma^{(6)}$ is also included in the above equation. It will be proved in this Appendix that this term is an order of magnitude smaller than the other terms for the parameter regime that we consider.

The time scale of the wave amplitude's evolution is assumed to be at least an order of magnitude larger than the time period of the wave. Therefore, $\partial a/\partial t$ will scale approximately as $\partial a/\partial t \sim \epsilon_t \epsilon_a \omega$. The amplitude's length scale is assumed to be much larger than the wavelength of the wave. Hence $\partial a/\partial x$ will scale as $\partial a/\partial x \sim \epsilon_x \epsilon_a \mathcal{K}/h$. Using the above scaling, the $\partial a/\partial x$ term in (B1) (including its coefficients) will scale as

$$2 \frac{\gamma^{(3)}}{\mathfrak{D}} \left(\frac{\mathcal{K}}{h} \frac{\partial a}{\partial x} \right) \sim \frac{1}{\omega} \frac{\gamma^{(3)} \mathcal{K}^2}{\gamma^{(1)} \mathcal{K}^2 - \gamma^{(2)}} \epsilon_x \epsilon_a \sim (\widehat{c}_g \epsilon_x) \omega \epsilon_a, \tag{B3}$$

where \widehat{c}_g represents the scale of group speed term for the packet, and is given by

$$\widehat{c}_g \equiv \frac{\omega^2 - f^2}{\omega^2} \left[\frac{\gamma^{(3)}}{(\omega^2 - f^2)\gamma^{(1)} + \gamma^{(3)}} \right]. \tag{B4}$$

It can be noticed that as ϵ_x is reduced, the effect of group speed diminishes as expected since a decrease in ϵ_x means the length scale of the packet is increased. Here, we also emphasize that for $\omega \approx N$, we have $\gamma^{(3)} \ll \omega^2 \gamma^{(1)}$. In such a parameter regime, $\widehat{c}_g \ll 1$, hence $\partial a/\partial x$ term will have a reduced effect on the amplitude evolution. Moreover, for $\omega \approx f$, similar behaviour is observed since $\widehat{c}_g \ll 1$.

Now we focus on the term containing $\gamma^{(6)}$ in (B1), which is (after some simplification)

$$\left(\frac{dh}{dx} \right)^2 \frac{\mathcal{W}}{\mathcal{K}^2} \frac{\omega a}{2}, \tag{B5}$$

where \mathcal{W} is a non-dimensional quantity defined as

$$\mathcal{W} = \frac{\omega^2 - f^2}{\omega^2} \frac{\gamma^{(6)}}{(\omega^2 - f^2)\gamma^{(1)} + \gamma^{(3)}}. \tag{B6}$$

The integral $\gamma^{(6)}$ is evaluated numerically to study its scaling. For uniform stratification, \mathcal{W} can be evaluated analytically as

$$\mathcal{W}_u = -\mathcal{M}^2 \left[\frac{\omega^2 - f^2}{\omega^2} \frac{N_b^2 - \omega^2}{N_b^2 - f^2} \right] \left(\frac{1}{3} - \frac{1}{2\mathcal{M}^2} \right), \tag{B7}$$

where \mathcal{W}_u is used to denote \mathcal{W} in constant stratification N_b , and $\mathcal{M} = n\pi$ is the non-dimensionalized vertical wavenumber of the wave. Moreover, using $(dh/dx)^2 \sim (\epsilon_h \epsilon_k)^2 \mathcal{K}^2$, the term given in (B5) will scale as

$$\left(\frac{(\epsilon_h \epsilon_k)^2}{2} \mathcal{W} \right) \omega \epsilon_a. \tag{B8}$$

Hence for the multiple-scale analysis to be consistent, $\mathcal{W}((\epsilon_h \epsilon_k)^2/2)$ has to be a small quantity. Figure 15 plots \mathcal{W} for nine stratification profiles, where $f = 0$ and $\omega/N_b = 0.4$ were used. In all panels, \mathcal{W}_u is also plotted for reference, where \mathcal{W}_u is evaluated with constant stratification N_b (hence \mathcal{W}_u is the same in all panels). From figure 15, it can be

Effects of mild-slope bathymetry on internal wave triads

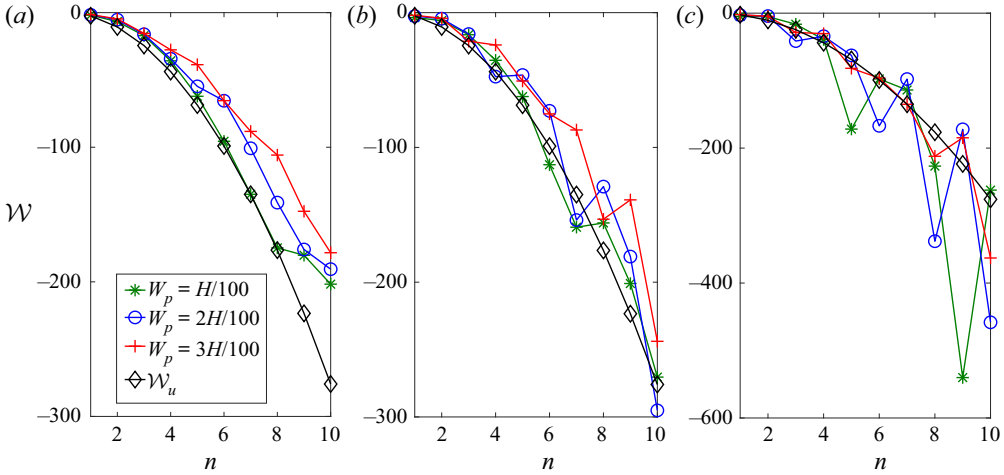


Figure 15. The variation in \mathcal{W} for modes 1–10 for different stratification profiles: (a) $N_{max} = 5N_b$ is used with $z_c = H/10$, and W_p is varied; (b) $N_{max} = 10N_b$ is used with $z_c = H/10$, and W_p is varied; (c) $N_{max} = 15N_b$ is used with $z_c = H/10$, and W_p is varied.

seen that in general for any stratification profile, \mathcal{W} is almost proportional to the square of the mode number n , similar to \mathcal{W}_u . Hence the bathymetry has to be more slowly varying (ϵ_k has to be smaller) as the mode number increases. Other pycnocline depths ($z_c = H/20, H/40, H/80$) were also tested for different combinations of W_p, N_{max} used in figure 15 that provided similar results.

The term that contains the $\gamma^{(5)}$ integral is now analysed. For all non-uniform stratification profiles used in this appendix, it was observed that

$$\gamma^{(5)} \lesssim \frac{1}{2}\gamma^{(3)}. \tag{B9}$$

Using (B9), the term containing $\gamma^{(5)}$ can be scaled to

$$\frac{1}{\mathfrak{D}_j} \left[\gamma^{(5)} \frac{2}{h} \frac{\partial h}{\partial x} \left(\frac{\mathcal{K}}{h} \right) a \right] \sim \left(\frac{\hat{c}_g}{2} \epsilon_h \epsilon_k \right) \omega \epsilon_a. \tag{B10}$$

Now we analyse how the wavenumber of a mode changes as h changes. To this end, (2.13b), which provides the n th eigenfunction, is differentiated in the x -direction, yielding

$$\left[\frac{\partial^2}{\partial \eta^2} + \mathcal{K}_n^2 \chi^2 \right] \frac{\partial \phi_n}{\partial x} = -\mathcal{K}_n^2 \frac{\partial \chi^2}{\partial x} \phi_n - \frac{d\mathcal{K}_n^2}{dx} \chi^2 \phi_n, \tag{B11}$$

where $\mathcal{K}_n = k_n h$. Equation (B11) can have a non-trivial solution only when the right-hand side is orthogonal to the solution of the self-adjoint operator on the left-hand side. Hence multiplying the right-hand side by ϕ_n , and then integrating in the η -direction between the domain limits, would result in

$$\frac{1}{k_n} \frac{dk_n}{dx} + \frac{1}{h} \frac{dh}{dx} = -\frac{1}{2\gamma_n^{(3)}} \int_{-1}^0 \frac{\partial N^2}{\partial x} \phi_n^2 d\eta. \tag{B12}$$

From (B12), we notice that the dimensional wavenumber k_n can change due to (i) change in the domain height, and (ii) change in the effective stratification profile. For uniform

stratification, $d\mathcal{K}_n/dx = 0$. For the lower modes (1–10) in profiles considered in this appendix, it was observed that

$$k_h \equiv O\left(\frac{1}{k_n} \frac{dk_n}{dx}\right) / O\left(\frac{1}{h} \frac{dh}{dx}\right) \sim O(1). \tag{B13}$$

Moreover, in general it was observed that as the mode number increases, k_h increases. Using (B13), the term containing the derivative of the wavenumber can be scaled as

$$\frac{1}{\mathfrak{D}_j} \left[\gamma^{(3)} \frac{dk}{dx} a \right] \sim \left(\frac{\widehat{c}_g}{2} \epsilon_h \epsilon_k \right) \omega \epsilon_a. \tag{B14}$$

We now evaluate $\gamma^{(4)}$ for the stratification profiles considered in this appendix. For modes 1–10, we find

$$\frac{\gamma^{(4)}}{\gamma^{(3)}} \sim O\left(\frac{1}{h} \frac{dh}{dx}\right). \tag{B15}$$

Using (B15), the term containing $\gamma^{(4)}$ can be scaled to

$$\frac{1}{\mathfrak{D}_j} \left[\frac{2\mathcal{K}}{h} \gamma^{(4)} a \right] \sim (\widehat{c}_g \epsilon_h \epsilon_k) \omega \epsilon_a. \tag{B16}$$

Using (B10), (B14) and (B16), we observe that for the lower modes, the three terms that comprise the β function can scale to a maximum value that is of the same order of magnitude. Hence they are all retained and are used in evaluating the β function (2.22). Moreover, it can be seen that the topographic terms are all dependent on the magnitude of the group speed. This relation is there naturally because a wave packet has to travel to different h fast enough to feel the effect of h variation. Scaling (B16) also holds for uniform stratification, where ϕ still varies in the x -direction. This is because of the nature of the ϕ normalization, i.e. (2.16), used in this paper.

The nonlinear coupling coefficient on the right-hand side cannot be further simplified, hence the nonlinear term scales as

$$\text{RHS of (B1)} \sim \widehat{\mathfrak{N}} \epsilon_a^2. \tag{B17}$$

Hence the final scaling for (2.24a)–(2.24c), using all the scalings derived, and with the inclusion of the $\gamma^{(6)}$ term, is (after some simplification)

$$\epsilon_t \sim \frac{\mathfrak{N}}{\omega} \epsilon_a - \widehat{c}_g \epsilon_x - \frac{(\epsilon_h \epsilon_k)^2}{2} \mathcal{W}. \tag{B18}$$

Here, an important point to remember is that the multiple-scale analysis was derived with the assumption that internal waves do not scatter/exchange energy to different modes of the same angular frequency. Therefore, the reduced-order equations provide the most accurate results when the internal waves do not scatter significant amount of their energy as they pass over a bathymetry. Moreover, even when $O(\epsilon_h \epsilon_k) \ll O(1)$ is satisfied, there could be special circumstances when waves may still get scattered significantly. An example of such a scenario is Bragg resonance of internal waves due to small-amplitude subcritical topographies (Buhler & Holmes-Cerfon 2011; Li & Mei 2014; Couston *et al.* 2017). Scattering/energy exchange can also occur for large-amplitude slowly varying topographies. However, it was observed that modes 1–8 are scattered

very little for large-amplitude topographies ($\epsilon_h \approx 0.5$) with low criticality ($\lesssim 0.1$) in the presence of uniform stratification. Criticality is defined as the ratio of the maximum slope of the topography to the slope of the internal wave. Mode-8 has $\approx 8\%$ variation in its amplitude as it propagates through a Gaussian topography with $\epsilon_h = 0.5$ and criticality = 0.1. Low-criticality topographies for mode- n of any ω/N_b are obtained when the condition $n\epsilon_k \ll O(1)$ is satisfied. Moreover, for the condition $n\epsilon_k \ll O(1)$, the last term in (B18) becomes an ϵ_k^2 term even for large-amplitude topographies. This can be seen by considering \mathcal{W}_u (which can also be used as a reference for non-uniform stratifications) given in (B7). Hence this term is neglected in the governing equations (2.24a)–(2.24c).

Appendix C. Scaling analysis of (6.8)

The scaling analysis of equation (6.8) has been done with the help of results derived in Appendix B. Equation (6.8) is re-written below for clarity:

$$\left[\left(\gamma_j^{(3)} \frac{\partial^2 \mathcal{A}_j}{\partial x^2} \right) + \mathcal{K}_j^2 \left(\frac{\mathcal{A}_j}{h^2} \gamma_j^{(3)} \right) \right] \mathcal{T}_j + 2 \left(\gamma_j^{(4)} - \frac{\gamma_j^{(5)}}{h} \frac{\partial h}{\partial x} \right) \frac{\partial \mathcal{A}_j}{\partial x} \mathcal{T}_j + \gamma_j^{(8)} \mathcal{A}_j \mathcal{T}_j + \left[\frac{\gamma_j^{(6)}}{h^2} \left(\frac{\partial h}{\partial x} \right)^2 - \frac{\gamma_j^{(5)}}{h} \left(\frac{\partial^2 h}{\partial x^2} \right) + \frac{2\gamma_j^{(5)}}{h^2} \left(\frac{\partial h}{\partial x} \right)^2 - 2 \frac{\gamma_j^{(7)}}{h} \frac{\partial h}{\partial x} \right] \mathcal{A}_j \mathcal{T}_j = \langle NL_3 \rangle. \quad (C1)$$

From here on, the subscripts are omitted, since the analysis is similar for both the waves. The leading-order terms scale as

$$\left[\frac{\partial^2 \mathcal{A}}{\partial x^2}, \mathcal{K}^2 \frac{\mathcal{A}}{h^2} \right] \sim \epsilon_a \frac{\mathcal{K}^2}{h^2}. \quad (C2)$$

Using (2.9), the scalings derived in Appendix B, and the small-amplitude assumption for topography ($\epsilon_h \ll O(1)$ and $\epsilon_k \sim O(1)$), we obtain

$$\left. \begin{aligned} 2 \frac{\gamma^{(4)}}{\gamma^{(3)}} \frac{\partial \mathcal{A}}{\partial x} &\sim 2\epsilon_h \epsilon_a \frac{\mathcal{K}^2}{h^2}, & \frac{2}{h} \frac{\partial h}{\partial x} \frac{\gamma^{(5)}}{\gamma^{(3)}} \frac{\partial \mathcal{A}}{\partial x} &\sim \epsilon_h \epsilon_a \frac{\mathcal{K}^2}{h^2}, \\ \left(\frac{1}{h} \frac{\partial^2 h}{\partial x^2} \right) \frac{\gamma^{(5)}}{\gamma^{(3)}} \mathcal{A} &\sim \frac{\epsilon_h}{2} \epsilon_a \frac{\mathcal{K}^2}{h^2}, & 2 \left(\frac{1}{h} \frac{\partial h}{\partial x} \right)^2 \frac{\gamma^{(5)}}{\gamma^{(3)}} \mathcal{A} &\sim \epsilon_h^2 \epsilon_a \frac{\mathcal{K}^2}{h^2}. \end{aligned} \right\} \quad (C3)$$

For the profiles and the parameters used in Appendix B, we observe that $(\omega^2 - f^2)\gamma^{(1)} + \gamma^{(3)} \sim \gamma^{(3)}$. Hence the $\gamma^{(6)}$ term can be scaled as

$$\frac{\gamma^{(6)}}{\gamma^{(3)}} \frac{1}{h^2} \left(\frac{\partial h}{\partial x} \right)^2 \mathcal{A} \sim \left(\mathcal{W} \epsilon_h^2 \right) \epsilon_a \frac{\mathcal{K}^2}{h^2}, \quad (C4)$$

where \mathcal{W} is plotted in figure 15 for various stratification profiles. Therefore, similar to Appendix B, the term $\mathcal{W} \epsilon_h^2$ has to be a small number for the multiple-scale analysis to be consistent. Furthermore, the $\gamma_j^{(7)}$ term was observed to scale as

$$\left(\frac{2}{h} \frac{\partial h}{\partial x} \right) \frac{\gamma^{(7)}}{\gamma^{(3)}} \mathcal{A} \lesssim \frac{\mathcal{K}_n^2}{\mathcal{K}_1^2} \left(\frac{1}{h} \frac{\partial h}{\partial x} \right)^2 2\epsilon_a, \quad (C5)$$

where \mathcal{K}_n is the non-dimensional wavenumber of wave-1 (or wave-3), and n gives the wave’s mode number. Note that this scaling has behaviour similar to that of \mathcal{W} , which is

nearly proportional to n^2 . Now we focus on the scaling of the integral $\gamma^{(8)}$:

$$\gamma^{(8)} = \left(\frac{dh}{dx}\right)^2 \int_{-1}^0 (N^2 - \omega^2)\phi \frac{\partial^2 \phi}{\partial h^2} d\eta + \frac{d^2 h}{dx^2} \int_{-1}^0 (N^2 - \omega^2)\phi \frac{\partial \phi}{\partial h} d\eta. \quad (C6)$$

For a uniform stratification, $\partial^2 \phi / \partial h^2 = 0$. Moreover, for the non-uniform stratification profiles used in Appendix B, it was observed that

$$\int_{-1}^0 (N^2 - \omega^2)\phi \frac{\partial^2 \phi}{\partial h^2} d\eta \lesssim \frac{\mathcal{K}_n^2}{\mathcal{K}_1^2} \frac{\gamma^{(3)}}{h^2}, \quad \int_{-1}^0 (N^2 - \omega^2)\phi \frac{\partial \phi}{\partial h} d\eta \sim \frac{\gamma^{(3)}}{h}. \quad (C7a,b)$$

Hence using (C7a,b), the scaling for $\gamma^{(8)}$ can be given in the simpler form

$$\gamma^{(8)} \sim \left[\frac{\mathcal{K}_n^2}{\mathcal{K}_1^2} \left(\frac{1}{h} \frac{dh}{dx}\right)^2 + \frac{1}{h} \frac{d^2 h}{dx^2} \right] \gamma^{(3)}. \quad (C8)$$

For low modes in the presence of small-amplitude topographies, the second term on the right-hand side of (C8) would be significantly higher than the first term. For any mild-slope bathymetry, the nonlinear terms $\langle NL_3 \rangle$ in (C1) can be scaled using the relation $d^n \mathcal{A} / dx^n \approx (\mathcal{K}/h)^n \mathcal{A}$, where $n \in \mathbb{Z}^+$. Using this approximation, the nonlinear term can be scaled as

$$\langle NL_3 \rangle \sim \frac{1}{\gamma^{(3)}} [NL_{(\nu,3)} + NL_{(B,3)} + NL_{(\psi,3)}] \epsilon_a^2. \quad (C9)$$

The nonlinear coupling coefficients cannot be simplified further. Moreover, the nonlinear terms have to be at least one order of magnitude less than the leading-order terms (given in (C2)).

REFERENCES

- ALAM, M.-R., LIU, Y. & YUE, D.K.P. 2009 Bragg resonance of waves in a two-layer fluid propagating over bottom ripples. Part 1. Perturbation analysis. *J. Fluid Mech.* **624**, 191–224.
- BAKER, L.E. & SUTHERLAND, B.R. 2020 The evolution of superharmonics excited by internal tides in non-uniform stratification. *J. Fluid Mech.* **891**, R1.
- BUHLER, O. & HOLMES-CERFON, M. 2011 Decay of an internal tide due to random topography in the ocean. *J. Fluid Mech.* **678**, 271–293.
- BURNS, K.J., VASIL, G.M., OISHI, J.S., LECOANET, D. & BROWN, B.P. 2020 Dedalus: a flexible framework for numerical simulations with spectral methods. *Phys. Rev. Res.* **2**, 023068.
- COUSTON, L.-A., LIANG, Y. & ALAM, M.-R. 2017 Oblique internal-wave chain resonance over seabed corrugations. *J. Fluid Mech.* **833**, 538–562.
- CRAIK, A.D.D. 1971 Non-linear resonant instability in boundary layers. *J. Fluid Mech.* **50** (2), 393–413.
- CRAIK, A.D.D., ADAM, J.A. & STEWARTSON, K. 1978 Evolution in space and time of resonant wave triads – 1. The ‘pump-wave approximation’. *Proc. R. Soc. A* **363** (1713), 243–255.
- DAVIS, R.E. & ACRIVOS, A. 1967 The stability of oscillatory internal waves. *J. Fluid Mech.* **30** (4), 723–736.
- GRIMSHAW, R. 1988 Resonant wave interactions in a stratified shear flow. *J. Fluid Mech.* **190**, 357–374.
- GRIMSHAW, R. 1994 Resonant wave interactions near a critical level in a stratified shear flow. *J. Fluid Mech.* **269**, 1–22.
- GRISOARD, N., STAQUET, C. & GERKEMA, T. 2011 Generation of internal solitary waves in a pycnocline by an internal wave beam: a numerical study. *J. Fluid Mech.* **676**, 491–513.
- GURURAJ, S. & GUHA, A. 2020 Energy transfer in resonant and near-resonant internal wave triads for weakly non-uniform stratifications. Part 1. Unbounded domain. *J. Fluid Mech.* **899**, A6.
- HALL, R.A., HUTHNANCE, J.M. & WILLIAMS, R.G. 2013 Internal wave reflection on shelf slopes with depth-varying stratification. *J. Phys. Oceanogr.* **43** (2), 248–258.
- HASSELMANN, K. 1967 A criterion for nonlinear wave stability. *J. Fluid Mech.* **30** (4), 737–739.

Effects of mild-slope bathymetry on internal wave triads

- INCE, E.L. 1956 *Ordinary Differential Equations*. Dover.
- KAFIABAD, H.A., SAVVA, M.A.C. & VANNESTE, J. 2019 Diffusion of inertia-gravity waves by geostrophic turbulence. *J. Fluid Mech.* **869**, R7.
- KIRBY, J.T. 1986 A general wave equation for waves over rippled beds. *J. Fluid Mech.* **162**, 171–186.
- KLYMAK, J.M., BUIJSMAN, M., LEGG, S. & PINKEL, R. 2013 Parameterizing surface and internal tide scattering and breaking on supercritical topography: the one- and two-ridge cases. *J. Phys. Oceanogr.* **43** (7), 1380–1397.
- KOUDELLA, C.R. & STAQUET, C. 2006 Instability mechanisms of a two-dimensional progressive internal gravity wave. *J. Fluid Mech.* **548**, 165–196.
- LAHAYE, N. & LLEWELLYN SMITH, S.G. 2020 Modal analysis of internal wave propagation and scattering over large-amplitude topography. *J. Phys. Oceanogr.* **50** (2), 305–321.
- LEGG, S. 2014 Scattering of low-mode internal waves at finite isolated topography. *J. Phys. Oceanogr.* **44** (1), 359–383.
- LEGG, S. & ADCROFT, A. 2003 Internal wave breaking at concave and convex continental slopes. *J. Phys. Oceanogr.* **33** (11), 2224–2246.
- LI, Y. & MEI, C.C. 2014 Scattering of internal tides by irregular bathymetry of large extent. *J. Fluid Mech.* **747**, 481–505.
- LIANG, Y., ZAREEI, A. & ALAM, M.-R. 2017 Inherently unstable internal gravity waves due to resonant harmonic generation. *J. Fluid Mech.* **811**, 400–420.
- MACKINNON, J.A., ALFORD, M.H., SUN, O., PINKEL, R., ZHAO, Z. & KLYMAK, J. 2013 Parametric subharmonic instability of the internal tide at 29°N. *J. Phys. Oceanogr.* **43** (1), 17–28.
- MACKINNON, J.A. & WINTERS, K.B. 2005 Subtropical catastrophe: significant loss of low-mode tidal energy at 28.9 degrees. *Geophys. Res. Lett.* **32** (15), L15605.
- MATHUR, M., CARTER, G.S. & PEACOCK, T. 2014 Topographic scattering of the low-mode internal tide in the deep ocean. *J. Geophys. Res.* **119** (4), 2165–2182.
- MAUGÉ, R. & GERKEMA, T. 2008 Generation of weakly nonlinear nonhydrostatic internal tides over large topography: a multi-modal approach. *Nonlinear Process. Geophys.* **15** (2), 233–244.
- MEYER, R.E. 1979 Surface wave reflection by underwater ridges. *J. Phys. Oceanogr.* **9** (1), 150–157.
- MUNK, W.H. 1966 Abyssal recipes. *Deep-Sea Res.* **13** (4), 707–730.
- OLBERS, D., POLLMANN, F. & EDEN, C. 2020 On PSI interactions in internal gravity wave fields and the decay of baroclinic tides. *J. Phys. Oceanogr.* **50** (3), 751–771.
- PHILLIPS, O.M. 1967 *The Dynamics of the Upper Ocean*. Cambridge University Press.
- SUTHERLAND, B.R. 2016 Excitation of superharmonics by internal modes in non-uniformly stratified fluid. *J. Fluid Mech.* **793**, 335–352.
- VARMA, D., CHALAMALLA, V.K. & MATHUR, M. 2020 Spontaneous superharmonic internal wave excitation by modal interactions in uniform and nonuniform stratifications. *Dyn. Atmos. Oceans* **91**, 101159.
- VARMA, D. & MATHUR, M. 2017 Internal wave resonant triads in finite-depth non-uniform stratifications. *J. Fluid Mech.* **824**, 286–311.
- VIC, C., GARABATO, A.C.N., GREEN, J.A.M., WATERHOUSE, A.F., ZHAO, Z., MÉLET, A., DE LAVERGNE, C., BUIJSMAN, M.C. & STEPHENSON, G.R. 2019 Deep-ocean mixing driven by small-scale internal tides. *Nat. Commun.* **10** (1), 2099.
- VOELKER, G.S., AKYLAS, T.R. & ACHATZ, U. 2021 An application of WKBJ theory for triad interactions of internal gravity waves in varying background flows. *Q. J. R. Meteorol. Soc.* **147** (735), 1112–1134.
- WUNSCH, S. 2017 Harmonic generation by nonlinear self-interaction of a single internal wave mode. *J. Fluid Mech.* **828**, 630–647.
- YOUNG, W.R., TSANG, Y.-K. & BALMFORTH, N.J. 2008 Near-inertial parametric subharmonic instability. *J. Fluid Mech.* **607**, 25–49.
- ZHAO, Z., ALFORD, M.H., GIRTON, J.B., RAINVILLE, L. & SIMMONS, H.L. 2016 Global observations of open-ocean mode-1 M2 internal tides. *J. Phys. Oceanogr.* **46** (6), 1657–1684.